

## Sum-Frequency Spectroscopy of a Monolayer of Zinc Arachidate at the Solid–Solid Interface

David A. Beattie,<sup>\*,†</sup> Ruchama Fraenkel, Sarah A. Winget, Adam Petersen, and Colin D. Bain<sup>‡</sup>

*Physical and Theoretical Chemistry Laboratory, University of Oxford,  
South Parks Road, Oxford, OX1 3QZ, UK*

*Received: October 28, 2005; In Final Form: December 6, 2005*

Infrared-visible sum-frequency spectroscopy has been used to record the vibrational spectrum of a zinc arachidate monolayer at the interface between a sapphire prism and a fused silica lens. Spectra have been recorded for the monolayer deposited on the prism before, during, and after contact, and as a function of increasing pressure. Sum-frequency spectra are reported of the monolayer under sliding contact. The monolayer is found to be resistant to pressure- and shear-induced conformational disorder. However, frequency shifts, drops in peak intensities, and changes in peak intensity ratios have been observed as the monolayer is placed in contact between the prism and the lens. Transfer of monolayer material between the two surfaces is observed and is confirmed by spectra obtained with a monolayer deposited on the surface of the lens rather than the prism. On one face of the sapphire prism, the monolayer reconstructs to a low symmetry layer, probably due to epitaxy. The epitaxial structure disappeared in contact. Existing models for calculating sum-frequency spectra have been extended to include unit cells containing two molecules and torsion about the terminal C–C bond. This model can explain some, but not all, of the experimental observations.

### Introduction

Organic monolayers play an important role in boundary lubrication.<sup>1,2</sup> Although the friction-reducing properties of organic boundary layers are well-known, the molecular basis of boundary lubrication remains poorly understood. Without an understanding of why particular molecules make effective lubricants one cannot rationally design boundary lubricants with improved performance or environmental characteristics.<sup>3</sup> The production of model organic monolayers through self-assembly<sup>4,5</sup> and Langmuir–Blodgett (L–B)<sup>6</sup> techniques provides us with the opportunity to study boundary lubricants in a controlled way. The surface force balance,<sup>7,8</sup> lateral force microscope,<sup>3,9,10</sup> and nanotribometer<sup>11</sup> have been used to relate friction on either a microscopic or macroscopic scale to the structure of the lubricating monolayer.

These mechanical measurements do not yield any direct information on the structure of the monolayers in the tribological contact. Molecular dynamics simulations cast some light on how organic monolayers respond to the extremes of pressure and shear in a solid–solid contact,<sup>12–20</sup> but an experimental probe of the in situ structure is an essential complement. One such technique is sum-frequency spectroscopy (SFS), a nonlinear form of vibrational spectroscopy that is well-suited for analyzing monolayers at buried interfaces.<sup>21–23</sup> The particular aspect of SFS that is useful for the study of boundary lubricants is not its intrinsic surface selectivity, since for a boundary lubricant one is interested in the structure of the entire lubricating film, but its exquisite sensitivity to conformational order in organic monolayers.

SFS has been used to characterize lubricant monolayers ex situ in order to relate structural differences between samples to their varying ability to decrease friction between rubbing surfaces.<sup>24,25</sup> But it is for in situ measurements that SFS offers the greatest promise. Characteristically, the first attempt to record a SF vibrational spectrum from a Langmuir–Blodgett monolayer in a solid–solid contact was made by Shen and co-workers.<sup>26</sup> They observed complete loss of SF signal from a monolayer of octadecyl alcohol on a quartz flat when the monolayer was placed in contact with a quartz lens and postulated that the molecules had either lain flat or become completely disordered under the applied pressure of 50 MPa. The first actual SF spectrum of boundary lubricant in situ was reported by Fraenkel et al. in 1998.<sup>27</sup> They used a total internal reflection (TIR) geometry to increase the signal level from a zinc arachidate L–B monolayer the solid–solid contact. They found that the monolayer retained a high degree of conformational order under load and observed no major structural changes in the contact. However, the overall signal intensity was more than an order of magnitude lower than expected based on a calculation of the optical field at the interface of the experiment, in agreement with the earlier observations of Du et al.<sup>26</sup> Fraenkel et al. suggested that the transfer of ordered patches of the monolayer to the counterface during contact could explain part of the observed drop in intensity, since the inversion of a molecule changes the phase of the induced SF field, which then cancels the field from molecules remaining on the substrate. A subsequent study by Beattie et al.<sup>28</sup> combined SFS and Raman spectroscopy, again using a TIR geometry to enhance signal levels in both spectroscopic techniques. The Raman spectra showed that a Zn arachidate monolayer was not displaced from the contact between a prism and a lens and that the conformational order in the monolayer was not affected by the applied pressure of 60 MPa, supporting the results from the accompany-

<sup>\*</sup> To whom correspondence should be addressed. E-mail: David.Beattie@unisa.edu.au.

<sup>†</sup> Current address: Ian Wark Research Institute, University of South Australia, Mawson Lakes, Adelaide, SA 5095, Australia.

<sup>‡</sup> Current address: Department of Chemistry, University of Durham, South Road, Durham DH1 3LE, UK.

ing SFS spectra. Intensity changes in polarized Raman spectra do, however, indicate that the chains tilt under large loads (200 MPa).<sup>29</sup>

Klennerman and co-workers extended the TIR approach with an SFS study of self-assembled monolayers of alkanethiols on a gold-coated bronze ball in contact with a sapphire prism.<sup>30,31</sup> They observed loss of SF signal in contact, analogously to earlier results on L–B monolayers, with a progressive decrease in signal with increasing pressure, and that the signal level was restored when contact was removed. The related technique of second harmonic generation (SHG) has also been applied to the problem of in situ tribology. Eisert et al. used TIR–SHG to study the orientation of *N*-[3-(trimethoxysilyl) propyl 2,4-dinitrophenylamine] molecules in a tribological contact.<sup>32</sup> They showed that the molecules adopted a radial tilt away from the center of the contact zone under load and preferential tilt in one direction under shear. They attribute the driving force for the reorientation to lateral forces induced by the squeezing of the monolayer film.

The results presented in this paper are an extension of our earlier work<sup>27,28</sup> on Zn arachidate monolayers on a sapphire prism. We compare SF spectra of monolayers before contact, in contact, and after contact and address issues of transfer of molecules between the two surfaces and the effect of varying pressure and of shear. Spectra are also presented of monolayers with an unusual structure that probably arises from epitaxy on a particular surface of the sapphire prisms used in this work. In an attempt to rationalize the experimental spectra in terms of the microscopic behavior of molecular films under pressure, we have developed a detailed model for the SF spectra from the terminal methyl group of the lubricant that does not assume free rotation of the methyl group. The aspects of the spectra that can be understood within this model, and those that cannot, are discussed. Some of our observations do not lend themselves to straightforward interpretation. However, from discussions with other researchers in the field we have come to appreciate that we are not the only group to obtain results that defy a simple explanation. We have chosen to include these puzzling data in this paper, partly to illustrate the enigmas that exist in sum-frequency experiments on confined monolayers, partly as encouragement to other researchers confronted by similar phenomena, but principally in the belief that rational physical explanations do underly our results, even if that explanation is not always apparent from the available evidence.

### Sum-Frequency Spectroscopy

SFS is a surface-specific form of vibrational spectroscopy based on the nonlinear optical effect of sum-frequency generation.<sup>33</sup> A fixed frequency visible or near-IR laser and a tunable infrared laser are focused onto the surface and the light emitted at the sum of the two incident frequencies is detected. SFG arises from a polarization of the surface,  $P^{(2)}$ , at the sum frequency ( $\omega_{\text{sum}} = \omega_{\text{vis}} + \omega_{\text{IR}}$ ):

$$P^{(2)}(\omega_{\text{sum}}) \chi^{(2)} : E_{\text{vis}} E_{\text{IR}} \quad (1)$$

where  $\chi^{(2)}$  is the second-order susceptibility of the surface and  $E_{\text{vis}}$  and  $E_{\text{IR}}$  are the electric fields of the visible and infrared lasers at the surface.  $\chi^{(2)}$  is a third-rank tensor whose 27 elements quantify the response of the sample to oscillating electric fields along orthogonal axes. These elements contain information on the structure, orientation, and density of the molecules at the surface. Different components of the susceptibility tensor are

sampled by changing the polarization of the incident beams and the detected SF light.

In general, several different components of  $\chi^{(2)}$  may add coherently to give the SF signal:

$$I_{\text{SFG}} \propto \left| \sum_{ijk} L_{\text{sum},i} K_{\text{vis},j} K_{\text{IR},k} \chi_{ijk}^{(2)} \right|^2 I_{\text{vis}} I_{\text{IR}} \quad (2)$$

where  $I_{\text{vis}}$  and  $I_{\text{IR}}$  are the intensities of the two incident lasers and  $L$  and  $K$  are the Fresnel coefficients for the infrared and visible lasers ( $K$ ),<sup>34</sup> and the emitted SF light ( $L$ ).<sup>35</sup> The Fresnel coefficients relate the amplitude and phase of a component of an electric field at the interface to the electric field in the incident or emitted laser beam. They depend on the angles of incidence and emission at the three wavelengths and on the refractive indices of the lens, prism, and monolayer (see Appendix A). The Fresnel coefficients, and thus the SFG intensity, are maximized if the lasers are incident at the critical angle for total internal reflection.

For a monolayer that is isotropic in the plane of the surface, only four combinations of the polarization of the incident and emitted light give rise to a SF spectrum: ssp, sps, pss, and ppp, where the letters denote the polarization of the SF, visible and infrared field, respectively. The first three of these polarization combinations sample a single nonzero element of the  $\chi^{(2)}$  tensor, while the ppp-combination depends on four components of  $\chi^{(2)}$ .

$$I_{\text{ssp}} \propto |\chi_{yyz}|^2 F_{yyz}^2 \quad (3)$$

$$I_{\text{sps}} \propto |\chi_{zyy}|^2 F_{zyy}^2 \quad (4)$$

$$I_{\text{pss}} \propto |\chi_{zzy}|^2 F_{zzy}^2 \quad (5)$$

$$I_{\text{ppp}} \propto |\chi_{xxz} F_{xxz} + \chi_{xzx} F_{xzx} + \chi_{zxx} F_{zxx} + \chi_{zzz} F_{zzz}|^2 \quad (6)$$

In eq 4–6,  $F_{ijk}$  represents the product of the individual Fresnel coefficients. Table 1 lists the values of  $F_{ijk}$  for the sapphire–air and sapphire–silica interfaces under the geometry of our experiment. When the SF visible and IR wavelengths are far from electronic resonances of the sample, the susceptibility tensor obeys Kleinman symmetry and the first two indices can be permuted without changing the value of the element. One consequence is that the pss and sps spectra differ only in the overall signal intensity arising from the differences in the Fresnel coefficients. The non-equivalence of the sps and pss spectra is prima facie evidence that the monolayer is not isotropic in the plane of the surface. This simplification is only true for optically isotropic substrates, since birefringent substrates mix s- and p-polarized light. Sapphire is not optically isotropic, but the magnitude of birefringence in sapphire is very small and the mixing of s- and p-polarization may be neglected.<sup>36</sup>

The second-order susceptibility is a macroscopic quantity that is related to the molecular hyperpolarizability,  $\beta$ , by

$$\chi^{(2)} = \frac{Nf}{\epsilon_0} \langle \beta \rangle \quad (7)$$

where  $N$  is the number of molecules per unit area,  $f$  is a “local field” correction to account for the additional electric field arising from the polarization of neighboring molecules, and the angle brackets indicate that  $\beta$  is averaged over the orientations of the molecule. Equation 7 provides the link between the response of the macroscopic sample ( $\chi^{(2)}$ ) and the response of the individual molecules ( $\beta$ ).

**TABLE 1: Resonant Frequencies, Line Widths, and Strengths (and spectral intensities) Observed for Zinc Arachidate at the Sapphire–Air and Sapphire–Silica Interface**

| resonance         | sapphire–air            |                         |                         |                               | sapphire–silica         |                         |                         |                               |
|-------------------|-------------------------|-------------------------|-------------------------|-------------------------------|-------------------------|-------------------------|-------------------------|-------------------------------|
|                   | $\omega/\text{cm}^{-1}$ | $\sigma/\text{cm}^{-1}$ | $\Gamma/\text{cm}^{-1}$ | $S_\nu (S_\nu^2)/\text{a.u.}$ | $\omega/\text{cm}^{-1}$ | $\sigma/\text{cm}^{-1}$ | $\Gamma/\text{cm}^{-1}$ | $S_\nu (S_\nu^2)/\text{a.u.}$ |
| <b>ssp</b>        |                         |                         |                         |                               |                         |                         |                         |                               |
| $r^+$             | 2877                    | 3                       | 2                       | 39 (1521)                     | 2875                    | 4                       | 2                       | 13 (169)                      |
| $r^+_{\text{FR}}$ | 2937                    | 4                       | 2                       | 33 (1089)                     | 2934                    | 4                       | 2                       | 8 (64)                        |
| $r^-_{\text{ip}}$ | 2967                    | 2                       | 2                       | −2 (4)                        |                         |                         |                         |                               |
| <b>sps</b>        |                         |                         |                         |                               |                         |                         |                         |                               |
| $r^-_{\text{ip}}$ | 2968                    | 3                       | 2                       | −12 (144)                     | 2968                    | 2                       | 2                       | −6 (36)                       |
| $r^-_{\text{op}}$ | 2957                    | 2                       | 2                       | 23 (529)                      | 2956                    | 2                       | 2                       | 15 (225)                      |
| <b>ppp</b>        |                         |                         |                         |                               |                         |                         |                         |                               |
| $r^-_{\text{ip}}$ | 2969                    | 2                       | 2                       | −21 (441)                     | 2965                    | 3                       | 2                       | 12 (144)                      |
| $r^-_{\text{op}}$ | 2957                    | 2                       | 2                       | 12 (144)                      | 2957                    | 2                       | 2                       | 12 (144)                      |
| $r^+$             | 2877                    | 4                       | 2                       | 21 (441)                      | 2876                    | 4                       | 2                       | 8 (64)                        |
| $r^+_{\text{FR}}$ | 2936                    | 4                       | 2                       | 21 (441)                      | 2934                    | 3                       | 2                       | 7 (49)                        |

Within the electric dipole approximation,  $\beta$  can be expressed in terms of the IR transition moment,  $\mu$ , and the Raman tensor,  $\alpha$ :<sup>33</sup>

$$\beta = \frac{\alpha\mu}{2(h/2\pi)(\omega_\nu - \omega_{\text{IR}} - i\Gamma_\nu)} \quad (8)$$

A vibration has to be both Raman and IR active to give rise to SFG. Consequently, centrosymmetric molecules are not SF active. A corollary for the present study is that only the terminal methyl vibrations ( $-\text{CH}_3$ ) will be observed for Zn-arachidate molecules with all-trans chains: the methylene ( $-\text{CH}_2$ ) modes are SF-inactive due to the local inversion symmetry of the chains. Introduction of gauche defects in the chains, which occur in disordered monolayers, breaks this symmetry and the methylene vibrations then give rise to SFG.

## Experimental Section

**(i) Sample Preparation.** The substrates forming the solid–solid interface were a plano-convex fused silica lens (diameter = 25.4 mm, radius of curvature = 154 mm, 10–5 scratch–dig,  $\lambda/10$  flatness; CVI Laser Corporation) and an equilateral sapphire prism (dimensions of  $15 \times 15$  mm, 20–10 scratch–dig,  $\lambda/20$  flatness; Crystran). Each optical component was placed in an ultrasonic bath for 10 min in alkaline detergent (DECON), high-purity water (Purite), acetone, methanol, and finally ultrahigh purity water (ELGA). The prism and lens were dried in a stream of dry  $\text{N}_2$  gas before being placed in the next solvent. The monolayer was deposited vertically on the prism using standard Langmuir–Blodgett techniques<sup>37,38</sup> in a NIMA 611 Langmuir trough. The dipping direction of the trough is in the plane of incidence of the laser beams used in the sum-frequency experiments. The aqueous subphase was a  $4 \times 10^{-4}$  mol  $\text{dm}^{-3}$  solution of  $\text{ZnSO}_4$  in ultrahigh purity water. Arachidic acid (Aldrich, 99.9% as a 1 mg  $\text{mL}^{-1}$  solution in chloroform) was spread on the surface of the trough from a syringe. The surface pressure of the monolayer was maintained at 30  $\text{mN m}^{-1}$  during deposition.

**(ii) Formation of Contact.** An AFM image of the flat surface of the fused silica lens yielded a RMS surface roughness of  $< 10$  Å, which we take to be indicative of the roughness of the curved surface. The RMS roughness of the sapphire prism was  $< 5$  Å. The prism was mounted on an X–Y translation stage (Newport UTMCC1DD, 1- $\mu\text{m}$  resolution) and the lens on a Z translation stage (UTMCC.1DD, 0.1- $\mu\text{m}$  resolution) (Figure 1). The stages are computer controlled with DC-servo drives, built-in tachometers, and linear position encoders. Pressure is applied by motion of the lens in the Z-direction (normal to the contact)

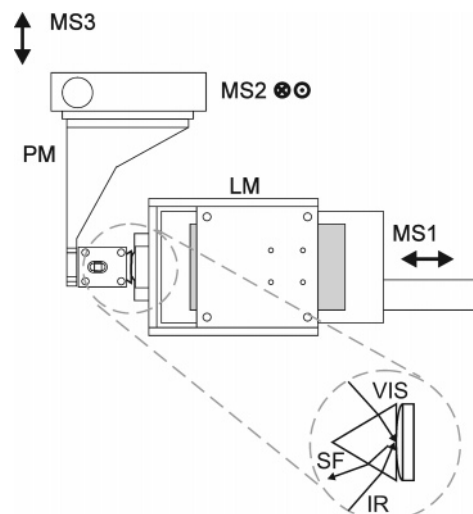


**Figure 1.** Top view of the motion stages and sample holders that make up the contact apparatus. MS1 = motion stage 1, MS2 = motion stage 2, MS3 = motion stage 3 (not shown), PM = prism mount, LM = lens mount. MS1 is used to move the lens into contact with the prism (Z-Axis), MS2 is used to shear the prism against the lens (Y-axis). MS3 (X-axis) is not used during the experiments. The circular blow-up section shows the arrangement of the lasers at the interface.

at a speed of  $10 \mu\text{m s}^{-1}$ . The lasers are incident in the X–Z plane. The prism and lens holders were designed so that the components could be removed and replaced with no need for realignment of the lasers. The average pressure in the contact was determined from measurement of the radius of the contact (Peak microscope,  $\times 100$  objective). The contact region was illuminated with white light from the back of the lens, allowing the determination of the diameter of the contact from Newton's rings.<sup>39</sup>

The radius of the contact,  $a$ , between a lens and a prism is given by<sup>40</sup>

$$a = \left( \frac{3FR}{4E} \right)^{1/3} \quad (9)$$

where  $R$  is the radius of curvature of the lens,  $F$  is the normal force (applied force + adhesion force), and  $E$  is the reduced Young's modulus of the two materials (given by  $1/E = ((1 - \sigma_1^2)/E_1) + ((1 - \sigma_2^2)/E_2)$  where  $\sigma_i$  and  $E_i$  are the Poisson ratio and Young's modulus of material  $i$ ;  $\sigma_{\text{sap}} = 0.25$ ,  $\sigma_{\text{sil}} = 0.17$ ,  $E_{\text{sap}} = 335$  GPa,  $E_{\text{sil}} = 73.1$  GPa). The pressure distribution within the contact region is of the form  $p(r) = p(0)(a^2 - r^2)^{1/2}$ , where the maximum pressure,  $p(0)$ , is given by:



$$p(0) = \frac{3F}{2\pi a^2} = \left( \frac{6FE^2}{\pi^3 R^2} \right)^{1/3} \quad (10)$$

The mean pressure,  $p_m = 2p(0)/3$ , is linearly proportional to the contact radius.

$$p_m = \frac{4Ea}{3\pi R} \quad (11)$$

Typical values for the mean pressure applied in this study ranged from 30 to 50 MPa. Shear was applied in a reciprocating fashion in the Y-direction with an amplitude of motion of 2.5 mm. The deadtime at the turnaround points was 50 milliseconds, and the acceleration to shear speed was  $1000 \mu\text{m s}^{-2}$ . Each spectrum took approximately 20 min to acquire, so each point on the contact line passed through the contact either 96 or 343 times for shear rates of  $200 \mu\text{m s}^{-1}$  and  $1 \text{ mm s}^{-1}$ , respectively. The alignment of the lasers was checked at both end points of the motion to ensure that both lasers were still in the contact region. No appreciable difference in the contact spot size or shape was observed between the top and bottom of the contact line, indicating that the normal pressure was constant during shearing.

**(iii) Sum-Frequency Spectrometer.** The sum-frequency spectrometer has been described in detail elsewhere.<sup>21</sup> The visible pulse (900  $\mu\text{J}$ , 3.5 ns, 20 Hz, 532 nm) was produced by second harmonic generation from a Q-switched Nd:YAG laser (Spectron, SL812). The output of a tunable dye laser (Spectron, SL 4000) was passed through a high-pressure hydrogen cell (26 bar, 22 passes) to generate the tunable infrared light (120  $\mu\text{J}$ ,  $\sim 1$  ns, 2800–3000  $\text{cm}^{-1}$ ) by stimulated Raman scattering.<sup>41</sup> The sum-frequency light was detected with a CCD (Princeton Instruments). The incident lasers were either s-polarized (parallel to the plane of the surface) or p-polarized (in the plane of incidence). A polarizer was placed in front of the CCD to select the polarization of the SF light (s- or p-polarized). SF spectra are labeled according to the polarization combination, e.g., ssp corresponds to s-polarized SF light, s-polarized visible light, and p-polarized infrared.

The green and infrared lasers were directed through the prism onto the contact between the prism and lens in a counter-propagating geometry (Figure 1). The angle of incidence at the sapphire–silica interface was  $55^\circ$  for both lasers, just below the critical angle,  $\theta_c$ , for both wavelengths ( $\theta_{c,\text{vis}} = 55.6$ ,  $\theta_{c,\text{IR}} = 55.9$ ). Incidence of the lasers at close to the critical angle at the solid–solid interface overcomes the problem of sensitivity in the experiment as the electric fields at an interface are maximized.<sup>28</sup> The lasers were focused onto the contact spot with a 30-cm focal length silica lens (532 nm) and a 25-cm focal length  $\text{CaF}_2$  lens (IR). Initial alignment of the lasers was performed by visual inspection. As the incident angles of the two lasers are below  $\theta_c$  for the sapphire–silica interface, but well above  $\theta_c$  for the sapphire–air interface, the green and IR beams show a noticeable decrease in intensity upon reflection from the contact spot.

The spectra were recorded at  $2 \text{ cm}^{-1}$  intervals with a 5 s exposure time at each wavelength (10 min per spectrum). The spectra were not normalized by the IR power. The spectra were fitted according to a procedure described elsewhere,<sup>42</sup> including homogeneous and inhomogeneous broadening in a single function. Each mode,  $\nu$ , was described by a Lorentzian function,  $S_\nu/(\omega_\nu - \omega_{\text{IR}} - i\Gamma_\nu)$ , where  $S_\nu$  is the line strength,  $\omega_\nu$  the resonant frequency,  $\Gamma_\nu$  the homogeneous line width, convoluted by a Gaussian function of half-width  $\sigma_\nu$ , to account for inhomogeneous broadening. The resulting function,  $f_\nu$ , is related

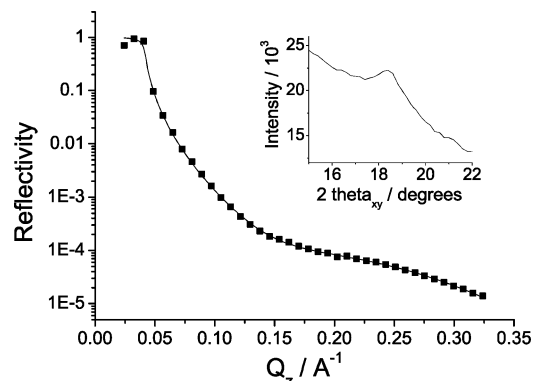


**Figure 2.** X-ray reflectivity curve of a monolayer of Zn arachidate on a sapphire prism. Inset is a GIXD diffraction peak for the monolayer.

to the Voigt profile,<sup>43,44</sup> which is widely used in gas-phase spectroscopy. The SF signal is then given by  $I_{\text{sf}} = |\sum f_\nu|^2$ . We did not include a nonresonant background in the fits.

## Results and Discussion

**(i) Monolayers at the Sapphire–Air Interface.** Monolayer samples were characterized by X-ray reflectometry and grazing incidence X-ray diffraction (GIXD) on beamline 16.2 at the Synchrotron Radiation Source at Daresbury (Warrington, UK). Figure 2 shows the reflectivity of a Zn arachidate monolayer on the sapphire prism as a function of the momentum transfer normal to the surface,  $Q_z (= (4\pi/\lambda)\sin\theta)$ , where  $\lambda$  was fixed at  $1.355 \text{ \AA}$  and the grazing angle was varied from 0 to  $1.5^\circ$ . The inset shows the in-plane diffraction peak at the specular angle for  $\theta_c$  (the critical angle for total external reflection). The reflectivity curve was modeled with Parratt32 software<sup>45</sup> and a three-layer model of air/hydrocarbon chain/ $\text{Al}_2\text{O}_3$ . The best fit to the reflectivity curve yielded a thickness of  $25 \text{ \AA}$  and a roughness of the substrate of  $< 1 \text{ \AA RMS}$ . In-plane diffraction measurements were limited by X-ray induced damage to the monolayer. Only a single peak was observed, corresponding to the (01) and (10) Bragg peaks at  $2\psi = 18.2^\circ$ . The scattering angle corresponds to a lattice vector of  $4.9 \text{ \AA}$  and an area per molecule of  $21 \text{ \AA}^2$ . The maximum in the  $Q_{xy}$  occurred close to the specular angle, which is indicative of upright chains. The X-ray reflectivity and GIXD data both point to a structure of the monolayer consisting of upright chains in a hexagonal lattice.

Figure 3 shows the SF spectra of a zinc arachidate monolayer at the sapphire–air interface for the ssp, sps, and ppp polarization combinations. The pss spectra differed from the sps spectrum only in the overall intensity. The theoretical fits shown in Figure 3 were used to determine the line strengths and resonant frequencies of the individual modes. The peaks in Figure 3 have been assigned on the basis of the vibrational spectroscopy of crystalline alkanes.<sup>46</sup> The major peaks in the ssp spectrum (Figure 3a) are assigned to the symmetric methyl stretch ( $r^+$ ,  $2877 \text{ cm}^{-1}$ ) and the Fermi resonance of the symmetric methyl stretch with an overtone of the  $\text{CH}_3$  bending mode ( $r^+_{\text{FR}}$ ,  $2937 \text{ cm}^{-1}$ ). The sps spectrum (Figure 3b) has only one major peak due to two overlapping components of the antisymmetric methyl stretch. The stronger component is the out-of-plane stretch ( $r^-_{\text{op}}$ ,  $2957 \text{ cm}^{-1}$ ) and the weaker component is the in-plane stretch ( $r^-_{\text{ip}}$ ,  $2968 \text{ cm}^{-1}$ ). The  $r^-_{\text{ip}}$  mode appears as a shoulder in the ssp spectrum, whereas the  $r^-_{\text{op}}$  mode is not required to fit the ssp spectrum. The ppp spectrum (Figure 3c) contains contributions from the  $r^+$  mode and both  $r^-$  modes. The two components of the antisymmetric stretch components are almost resolved, with the high frequency in-plane mode

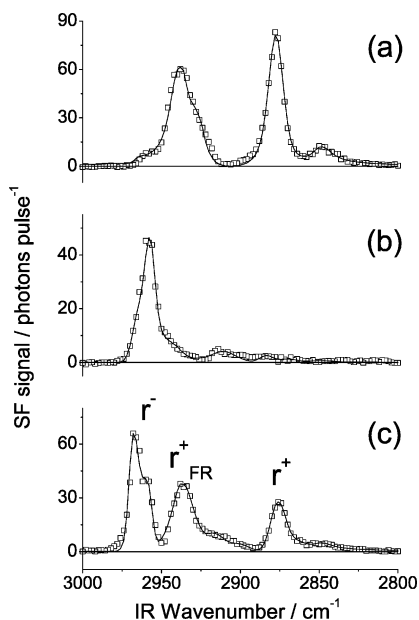


**Figure 3.** Sum-frequency spectra of zinc-arachidate at the sapphire–air interface recorded using (a) ssp, (b) sps, and (c) ppp polarization combinations. The lasers were incident on the prism face well above the total internal reflection angle for the sapphire–air interface. The open squares ( $\square$ ) are the data points and the solid line (—) is the simulation of the peak intensities.

being more intense. The methylene modes of disordered hydrocarbon chains give rise to peaks around  $2920\text{ cm}^{-1}$  (antisymmetric stretch,  $d^-$ ),  $2850\text{ cm}^{-1}$  (symmetric stretch,  $d^+$ ), and  $2930\text{--}2890$  ( $d^+$  Fermi resonance), of which the  $d^+$  mode is normally the best resolved in SF spectra.<sup>47</sup> These peaks are weak in the spectra in Figure 3, which is indicative of hydrocarbon chains in a predominantly all-trans chain conformation, with only a small number of gauche defects. The amplitude of the  $d^+$  peak is somewhat variable from sample to sample, suggesting that it arises principally from sample defects (e.g., at grain boundaries) rather than being intrinsic to the monolayer phase.

The ratio of intensities of the  $r^+$  mode in ssp and sps spectra has frequently been used to calculate the orientation of the terminal methyl group.<sup>48</sup> In the sps spectrum, the  $r^+$  mode is weak and not sufficiently well-resolved to permit such a determination with any confidence.

**(ii) Monolayers at the Sapphire–Silica Interface.** Figure 4 shows the SF spectra of zinc arachidate at the sapphire–silica interface at a mean contact pressure of 34 MPa. It is straightforward to establish that the SF signal originates from surfaces that are in optical contact. Direct visualization of the Newton's rings and the scattered green light shows that the green beam is confined within the contact region. The location of the IR beam can be deduced from the reflected intensity. Since the angles of incidence are above the critical angle,  $\theta_c$ , for the sapphire–air interface and just below  $\theta_c$  for the sapphire–silica interface, the reflectivity decreases when the laser beams fall in the region of contact between the prism and lens. For both beams, a flat minimum is observed in the reflected intensity when the laser spot is tracked across the region of contact, indicating that the diameter of the laser beam is smaller than the contact diameter. The surface roughness of the lens and the prism are both less than the thickness of the monolayer, implying that the monolayer is also in mechanical contact with the counterface. Any occasional asperities on the surface that are higher than the thickness of the monolayer will deform under the applied load.<sup>26</sup>

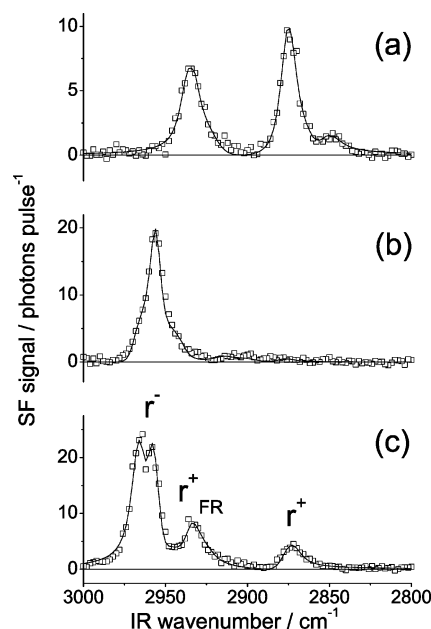


**Figure 4.** Sum-frequency spectra of zinc-arachidate at the sapphire–silica interface recorded using (a) ssp, (b) sps, and (c) ppp polarization combinations. The open squares ( $\square$ ) are the data points and the solid line (—) is the simulation of the peak intensities.

The in-contact spectra in Figure 4 have been fitted to obtain line strengths and resonant frequencies of the individual modes (Table 1). The principal point of comparison of the in-contact spectra (Figure 4) with the pre-contact spectra (Figure 3) is the overall similarity, apart from a general decrease in the signal levels in contact. There are, however, several minor differences. First, the  $r^+$  and  $r^+_{\text{FR}}$  modes show small red shift ( $1\text{--}3\text{ cm}^{-1}$ ) in contact. Red shifts of a similar magnitude ( $2\text{--}4\text{ cm}^{-1}$ ) have been seen in the SF spectra of self-assembled monolayers on gold when they are immersed in liquids<sup>49</sup> and in the IR spectra of monolayers in contact with liquids.<sup>50</sup> These peak shifts probably arise from the change of environment of the methyl group when the contacting medium changes from air to silica.

Second, the  $r^-_{\text{ip}}$  mode in the ssp spectrum disappears in contact. This would suggest a change in orientation of the terminal methyl group. Third, the relative intensities of the  $r^+$  and the two  $r^-$  modes in the ppp spectrum are different. The interpretation of these changes is complicated by the different weighting of the four susceptibility components in the pre-contact and in-contact spectra. The values of the Fresnel coefficients in Table 1 show that  $\chi_{xxz}$ ,  $\chi_{zzz}$  and  $(\chi_{zxx} + \chi_{xzx})$  have comparable weightings in the pre-contact spectrum (where the angle of incidence is far above the critical angle), while the in-contact spectrum is dominated by  $\chi_{zzz}$ .

The overall signal drop seen in the in-contact ssp, sps, and ppp spectra was not expected on the basis of the calculated Fresnel coefficients for the two interfaces (see Table 2). For the ssp and sps spectra, which depend only on a single Fresnel coefficient, the SF spectra at the sapphire–silica interface are expected to be 2–3 times stronger than at the sapphire–air interface (compare  $|F_{ijk}|^2$  at the two interfaces), yet in Figure 4 the spectra are much weaker than at the sapphire–air interface. The absolute signal levels in-contact are quite variable and they are sometimes more intense than pre-contact (e.g., see Figure 6a), but they are always much weaker than expected based on the Fresnel coefficients. In the case of the ssp polarization combination, the average in-contact signal drop from six different experiments is 78%, with a standard deviation of 8%. The values of the average drop in the in-contact signal for the

**TABLE 2: Fresnel Coefficients for the Sapphire–Air and Sapphire–Silica Interface<sup>a</sup>**

| $F_{ijk}$  | sapphire–air  | sapphire–silica                  |
|------------|---|----------------------------------|
| <b>ssp</b> |   |                                  |
| $F_{yyz}$  | $(-1.80 + i1.01)$<br>$F_{yyz} \cdot F_{yyz}^* = 4.26$ | $-3.18$<br>$(F_{yyz})^2 = 10.11$ |
| <b>sps</b> |   |                                  |
| $F_{zyz}$  | $(1.60 - i0.98)$<br>$F_{zyz} \cdot F_{zyz}^* = 3.52$  | $3.30$<br>$(F_{zyz})^2 = 10.89$  |
| <b>pss</b> |   |                                  |
| $F_{zyy}$  | $(2.39 - i2.09)$<br>$F_{zyy} \cdot F_{zyy}^* = 10.08$ | $2.19$<br>$(F_{zyy})^2 = 4.80$   |
| <b>ppp</b> |   |                                  |
| $F_{xxz}$  | $(0.42 - i1.20)$                                      | $0.29$                           |
| $F_{xzx}$  | $(-0.38 - i1.07)$                                     | $-0.38$                          |
| $F_{zxx}$  | $(-0.76 + i2.15)$                                     | $0.05$                           |
| $F_{zzz}$  | $(-0.34 + i0.96)$                                     | $-2.54$                          |

<sup>a</sup> The values used for the refractive indices were IR: sapphire – 1.69, silica – 1.40, monolayer – 1.45. visible: sapphire – 1.77, silica – 1.46, monolayer – 1.50. SF: sapphire – 1.78, silica – 1.46, monolayer – 1.50.

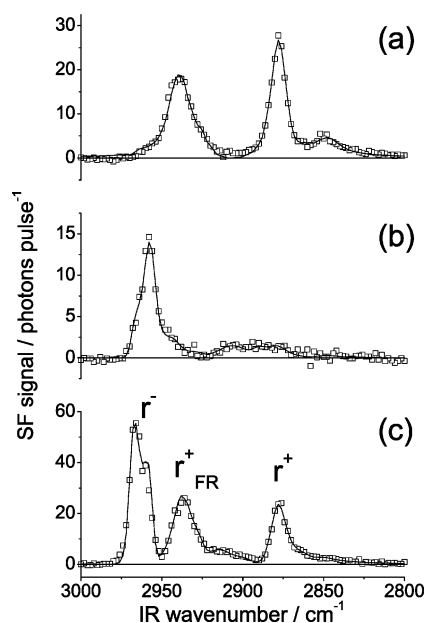


**Figure 5.** Post-contact sum-frequency spectra of zinc-arachidate at the sapphire–air interface recorded using (a) ssp, (b) sps, and (c) ppp polarization combinations. The open squares ( $\square$ ) are the data points and the solid line ( $-$ ) is the simulation of the peak intensities.

other two polarization combinations are slightly different, but the trend is the same; the in-contact signal levels are much lower than expected.

The observation of unexpectedly weak in-contact spectra is entirely consistent with previous data from our groups and others<sup>26–28,30,31</sup> but still does not have a satisfactory explanation. To add to the puzzle, s-polarized Raman spectra of the same monolayer at the  $\text{CaF}_2/\text{air}$  and  $\text{CaF}_2/\text{MgF}_2$  interface<sup>28</sup> showed a 10-fold increase in signal in contact, in agreement with the calculated Fresnel coefficients for the two interfaces. A comparison with the Raman data (albeit for different substrates) suggests that the loss of SF signal in-contact does not arise from gross errors in the calculation of the macroscopic interfacial electric fields but from some change in structure of the monolayer: the s-polarized Raman spectra are dominated by the  $\text{CH}_2$  modes of the hydrocarbon backbone and are much less sensitive than the SF spectra to molecular structure.

There are a number of possible explanations for the in-contact signal drop. First, the monolayer could be expelled from the

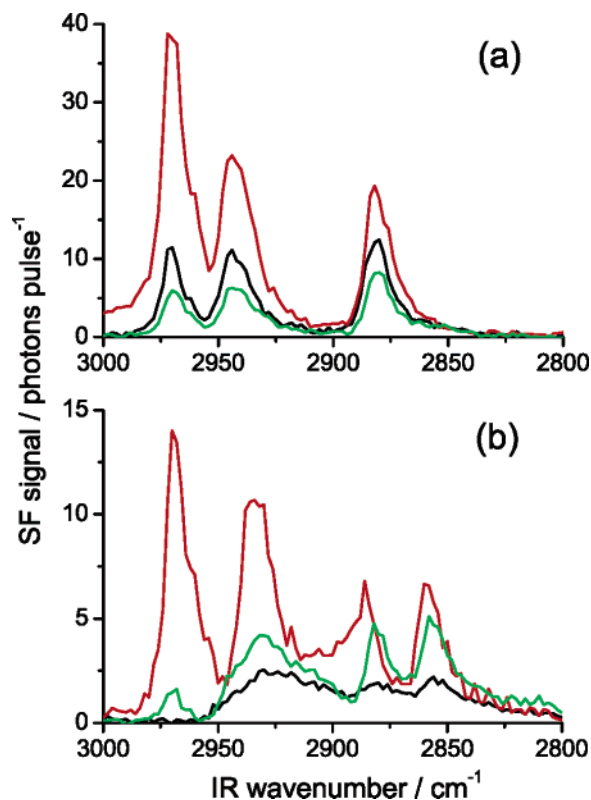


**Figure 6.** (a) ppp spectra of a sapphire prism “pre” (black), “in” (red) and “post” (green) contact with a fused silica lens applying an average pressure of  $\sim 30$  MPa to the prism, with a protonated monolayer of zinc arachidate on the prism and a clean lens and (b) ppp spectra of a clean prism surface and a protonated monolayer of zinc arachidate on the lens, “pre” (black), “in” (red) and “post” (green) contact.  $0.3 \text{ mJ pulse}^{-1}$  at  $532 \text{ nm}$  ( $\theta_i = 61^\circ$ ) and  $0.4 \text{ mJ pulse}^{-1}$  in the IR ( $\theta_i = 56.5^\circ$ ).

contact. This explanation is inconsistent with the preservation of the signal in the Raman experiments and the observation of Du et al.<sup>26</sup> that the SF signal recovered completely after the counterface was removed. Second, the molecules could change their orientation and lie parallel to the surface. Since the applied pressures are negligible compared to the bulk modulus of the monolayer, such reorientation would involve detaching the headgroups from the silica surface and forming multilayers of chains parallel to the substrate. There is no obvious physical reason for such a reorganization, it is inconsistent with polarized Raman spectra at comparable pressures and would not result in the recovery of the SF signal after the contact was removed. Third, the molecules could completely disorder so that orientational average  $\langle \beta \rangle$  vanished. Such a drastic structural change would result in a large number of gauche defects and an increase in the intensity of the methylene modes relative to the methyl modes in the SF spectra. Yet the spectra are qualitatively unchanged. Furthermore, a conformationally disordered film would have a larger volume than the initial organized monolayer and would not be created by pressure alone, but could conceivably be caused by shear. Such a shear-induced conformational change is unlikely to be reversible. Once again, Raman spectra show that the monolayer remains conformationally ordered in contact. Fourth, patches of monolayer could be transferred to the counterface. Transfer of a Langmuir–Blodgett film was observed as early as 1954,<sup>51</sup> and more recently, islands of bilayers have been moved around on surfaces with an AFM tip while retaining their structure.<sup>52</sup> The most likely cause of monolayer transfer would be microslip. As a result of the different geometries and elastic properties of the materials forming the prism and the lens, the two surfaces in contact do

not deform equally and so there is slip of one relative to the other.<sup>40</sup> Since the methyl groups in the transferred monolayer would have an inverted orientation, they would cancel the signal from the initial monolayer. The SF signal would then scale as  $(1-2f)^2$ , where  $f$  was the fraction of the monolayer transferred to the opposing substrate. The observed loss of intensity in contact would require  $f \sim 0.4$ . The residual signal after contact was removed would be proportional to  $(1-f)^2$ , and would be predicted to be only 30% or so of the original signal. This mechanism can therefore not explain the observation of complete signal recovery after contact by Du et al.<sup>26</sup> In our experiments, partial loss of signal was observed, so we investigated this possibility further.

**(iii) Post-Contact Spectra and Monolayer Transfer.** Figure 5 shows SF spectra of a Zn arachidate monolayer after the lens has been removed from the prism. (The spectra shown in Figures 3–5 with the same polarization combination were taken on the same sample; different polarization combinations were taken on different samples.) The spectra are qualitatively the same as those recorded from a fresh monolayer (Figure 3): the ssp spectrum regains a shoulder due to the  $\nu_{\text{ip}}^-$  mode, there is no increase in the  $\text{d}^+$  mode implicating conformational disorder, and the relative peak intensities in the ppp return to those that were observed for the fresh monolayer. The major difference between the pre-contact and post-contact spectra is in overall signal level: the post-contact spectra are all weaker. The extent of recovery is variable from sample to sample. For the six repeat experiments performed using the ssp polarization combination, the mean post-contact signal was 45% of the initial (pre-contact) level, with a standard deviation of 16%. In addition, for a given sample, the extent of recovery may vary among the different polarization combinations, indicating that there has been some change in the structure of the monolayer. No correlation was observed between the level of in-contact signal drop and the level of recovery after contact was removed.

To investigate the possibility of monolayer transfer, we compared pre-, in-, and post-contact SF spectra for samples in which the monolayer was deposited on the prism with those in which it was deposited on the lens (Figure 6). The solid black line in Figure 6b shows the SF spectrum of the bare sapphire prism. It shows broad and poorly resolved features in the 2850–2950  $\text{cm}^{-1}$  region that are indicative of adventitious contamination, which is unavoidable for high-energy surfaces exposed to a laboratory environment. The prism was then brought into contact with a silica prism coated with a L–B monolayer of Zn arachidate and a spectrum from the monolayer on the lens is observed (red line in Figure 6b). After the lens has been removed (green line in Figure 6b) the SF signal decreased but not back to the pre-contact level, indicating the transfer of material from the lens to the prism. There is no reason to believe that the amount of transfer from the prism to the lens should be the same as from the lens to the prism, but the spectra shown are consistent with 20–30% of a monolayer being transferred. We note in passing that the interpretation of the SF intensity from patches of transferred monolayer depends on the size of the patches. If the patches are smaller than the coherence length of the experiment, then the SF field will be proportional to  $f$  and the signal to  $f^2$ . If they are larger than the coherence length, different patches will add incoherently and the signal will be proportional to  $f$ .

One puzzling feature of the spectra in Figure 6 is that the in-contact spectrum is much weaker for the monolayer on the lens than on the prism and contains prominent methylene bands, which are indicative of conformational disorder in the mono-

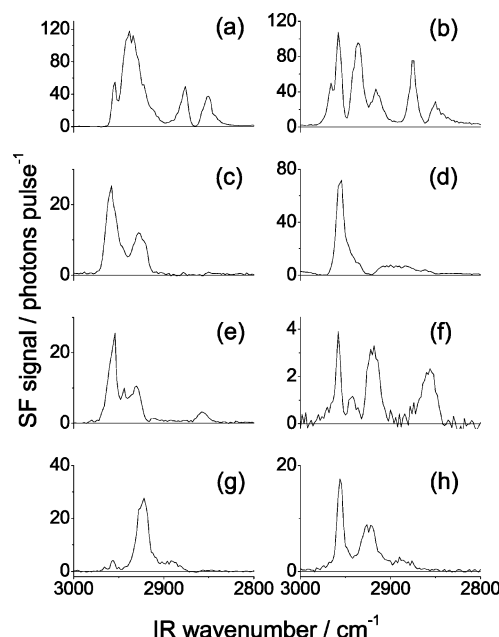


**Figure 7.** (a) ssp, (b) ppp, (c) sps, (d) pss, (e) sss, (f) pps, (g) spp, and (h) psp spectra of zinc-arachidate on the third face of the sapphire prism.

layer. We have no reason to believe that the initial monolayer on the silica lens is more disordered than on the sapphire prism (silica is a suitable substrate for L–B transfer), though we cannot readily characterize the monolayer on the curved surface of the lens.

The data in Figure 6 show that transfer of the monolayer from the prism to the lens could be responsible for part of the signal loss observed “in-contact” in our experiments and for the incomplete recovery of the signal after the lens is removed. Du et al.<sup>26</sup> observed no post-contact loss of signal in their experiments at the silica–silica interface, where there is much less slip since the Young’s moduli of the two surfaces are identical. This observation supports the microslip mechanism as being the cause transfer of monolayer material in our system, but equally demonstrates that monolayer transfer cannot be the sole mechanism responsible for the large drop in signal in-contact.

**(iv) Epitaxial Effects.** The sapphire prisms used in these experiments were not cut in any particular orientation with respect to the crystallographic axes. While two faces of each sapphire prism gave spectra that were consistent with the upright hexagonal phase observed by X-ray scattering, the third face yielded more complex spectra, including nonzero signals for the polarization combinations sss, spp, psp, and pps, which are forbidden for a monolayer that is isotropic in the plane of the surface. It is perhaps not very surprising that an LB monolayer should reconstruct in contact with certain crystal faces in order to maximize the electrostatic interactions between the carboxylate headgroups and the charges on the surface of the sapphire. What is of interest for this paper is how this “epitaxial” monolayer behaves in a tribological contact. Figure 7 shows all eight polarization combinations for a Zn arachidate monolayer on sapphire in air. The four polarization combinations (sss, psp, pps, and spp) shown in Figure 7e–h would have no intensity if the monolayer were isotropic in the plane or if the only anisotropy were along the dipping direction for the L–B transfer (the X direction). The fact that all four of these “forbidden” combinations are nonzero shows that this monolayer is not isotropic in the plane of the surface and that the X–Z plane is not a plane of symmetry. The inequivalence of the spp



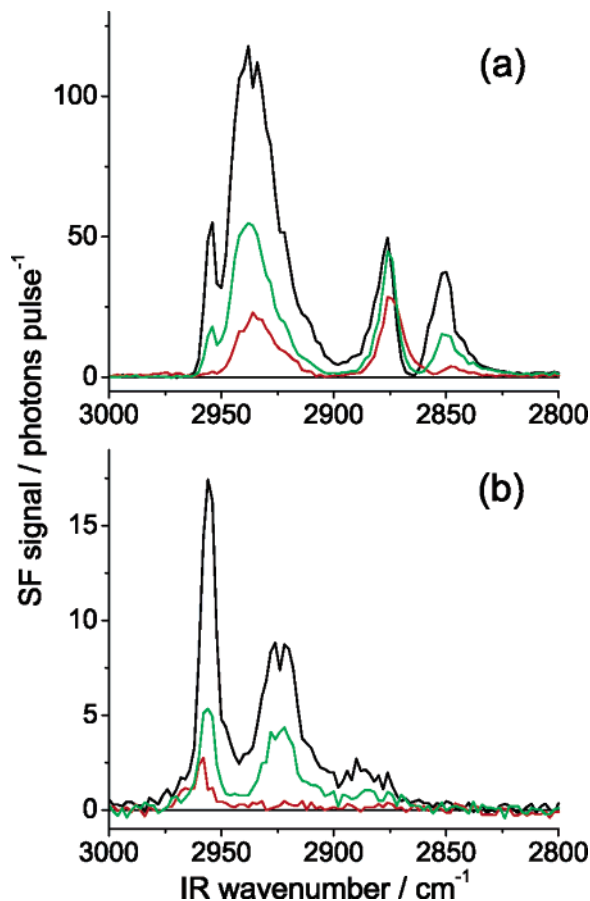


**Figure 8.** Pre- (black), in- (red), and post-contact (green) of zinc arachidate on the third face of the sapphire prism using (a) ssp, and (b) psp polarization combinations.

and pss spectra (Figure 7c and d) shows further than the Y–Z plane is not a plane of symmetry (otherwise they would both be determined only by  $\chi_{zyy} = \chi_{yzy}$ ). In addition to the methyl modes observed in Figures 3–6, the spectra in Figure 7 also contain peaks that can be assigned to  $\text{CH}_2$  stretching vibrations ( $2920\text{ cm}^{-1}$  ( $\text{d}^-$ ) and  $2850\text{ cm}^{-1}$  ( $\text{d}^+$ )). The presence of  $\text{CH}_2$  vibrations in SF spectra is often an indication of disorder in the monolayer and is then associated with a decrease in the strength of the  $\text{CH}_3$  modes. In this case, however, the appearance of  $\text{CH}_2$  modes is associated with changes in the relative intensities of the  $\text{CH}_3$  modes, but no general decrease (compare Figure 3 with Figure 7a–c).

The effect of pressure on this epitaxial monolayer is shown in Figure 8 for ssp and psp polarizations. The former polarization combination is allowed for monolayers that are isotropic in the surface plane while the latter is forbidden. The ssp spectrum in air contains a strong sharp  $\text{r}_{\text{op}}^-$  peak at  $2955\text{ cm}^{-1}$  and a  $\text{d}^+$  peak at  $2850\text{ cm}^{-1}$ . The former peak disappears almost completely in contact while the latter loses most of its intensity. The in-contact spectrum closely resembles the spectra from the other two faces of the prism (compare Figure 8a and Figure 4a). For the psp polarization, the dominant  $\text{r}_{\text{op}}^-$  peak at  $2955\text{ cm}^{-1}$  loses 90% of its intensity in contact and shifts to higher wavenumber; the other peaks disappear completely. Upon withdrawal of the lens, there is only partial recovery of the “epitaxial” features in each spectrum. Figure 9 shows in-contact spectra for the pss and sps polarizations matching in shape, as would be expected for a monolayer with mirror symmetry in the YZ plane. It should be noted that the observation of epitaxial structure, the subsequent loss of epitaxial structure in-contact,

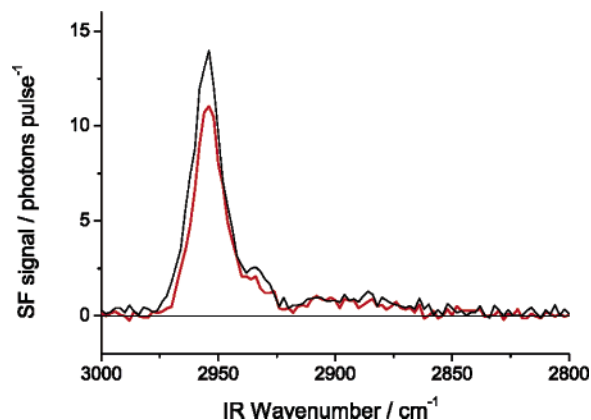


**Figure 9.** In-contact spectra of sps (black) and pss (red) spectra of zinc-arachidate.

and the partial recovery of the epitaxial structure post-contact were entirely reproducible over five separate experiments.

We interpret the above results as follows. The Langmuir monolayer on the surface of water at the transfer pressure is probably in the LS or S phase.<sup>53</sup> During the deposition process, the Langmuir film can reconstruct in order to optimize the interactions between the monolayer and the substrate. On two of the faces, an upright hexagonal phase forms, while the third face imposes a complex, low symmetry structure on the monolayer. Similar behavior was observed previously for stearic acid adsorbed on the (10 $\bar{1}$ 4) cleavage face of calcite, a crystal surface with no symmetry elements.<sup>36</sup> The lack of symmetry in the calcite surface was repeated in the monolayer: all eight possible polarization combinations yielded SF spectra that varied strongly with the azimuthal angle of the substrate. Analogously, the strong, sharp peaks in the SF spectra of zinc arachidate on sapphire suggest a low symmetry, densely packed monolayer containing specific conformational defects. The structure adopted by the monolayer is a compromise between the optimum headgroup arrangement and efficient packing of the tail groups. The all-trans upright hexagonal or pseudohexagonal phase is a common packing motif in Langmuir monolayers (where it is labeled the LS phase) and is also adopted by some linear alkanes near their melting point.<sup>54</sup> Where interactions with the substrate dictate a different headgroup spacing, the chains adopt a less dense packing with conformational defects in order to adapt to the headgroup lattice. When the lens is brought into contact with the monolayer, the increase in pressure tips the balance of interactions toward a structure with efficient packing of the tail groups, resulting in a change of the monolayer phase from the epitaxial to the pseudohexagonal structure and the loss of the signal from the forbidden polarizations. Upon release of the pressure, the monolayer only partially reconstructs back to the epitaxial structure, probably due to kinetic limitations.

The determination of the structure of this epitaxial monolayer would be a major project on its own and is of little relevance to the main thrust of this work. We can, however, draw two useful conclusions from the behavior of the epitaxial monolayer. The first is that pressure can induce (at least partially) reversible phase changes in boundary lubricants. Phase changes in lubricant films have been invoked to explain tribological phenomena such as stick–slip<sup>8,55,56</sup> and also provide a dissipation mechanism in rolling or sliding friction. The second is that the almost complete disappearance of the forbidden spectra under pressure provides strong evidence that a large fraction ( $\geq 80\%$ ) of the molecules in the contact region are in actual mechanical contact with the counterface. Without actual mechanical contact, there is no driving force for the reconstruction of the monolayer.



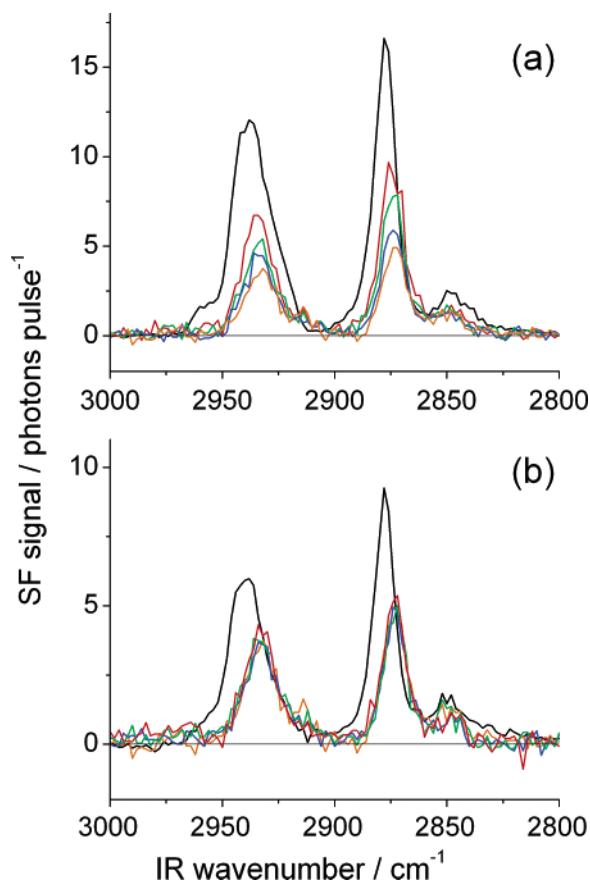


**Figure 10.** (a) ssp sum-frequency spectra of zinc-arachidate at the sapphire-silica interface recorded with increasing pressure: 32.5 (red), 37.7 (green), 41.5 (blue), and 44.5 (orange) MPa. The pre-contact spectrum (black) is included for comparison (divided by 5). (b) ssp sum-frequency spectra of zinc-arachidate at the sapphire-silica interface recorded with decreasing pressure: 44.5 (orange), 41.5 (blue), 37.7 (green), and 33.9 (red) MPa. The black line is the post-contact spectrum (divided by 3).

#### (v) Spectra Recorded with Varying Pressure and Shear.

Figures 3–9 show the effect of a static contact on the structure of the monolayer, possibly influenced by microslip during the formation of the contact. In a moving contact, which is more representative of the processes that occur in a real mechanical device, the pressure ramps up and then down (in a rolling or sliding contact), and in the sliding contact the interface is additionally subject to high rates of shear. For this reason we have investigated the SF spectra of the monolayer as a function of varying pressure and shear. The effect of changing the applied force (and hence the mean pressure) on the SF spectra is shown in Figures 10 and 11. The mean pressure in the contact scales as the one-third power of the applied force (eqs 10 and 11), so only relatively small pressure ranges are covered through variation of the force on a lens of given curvature (larger pressure ranges are covered with lenses of different curvature,  $R$ ). However, the use of only one lens allows us to follow the effects of increasing and decreasing pressure on the same monolayer sample.

Figure 10 shows ssp spectra of a Zn arachidate monolayer at the sapphire–silica interface as a function of increasing (Figure 10a) and decreasing (Figure 10b) pressure in the range  $p_m = 32$  MPa – 44 MPa. The pre-contact (Figure 10a) and post-contact spectra (Figure 10b) are also shown. The most obvious feature of the spectra in Figure 10 is the pronounced red shift of the peaks in contact compared to the pre- and post-contact spectra. The relative intensity of the  $r^+$  and  $r^+_{FR}$  modes remains

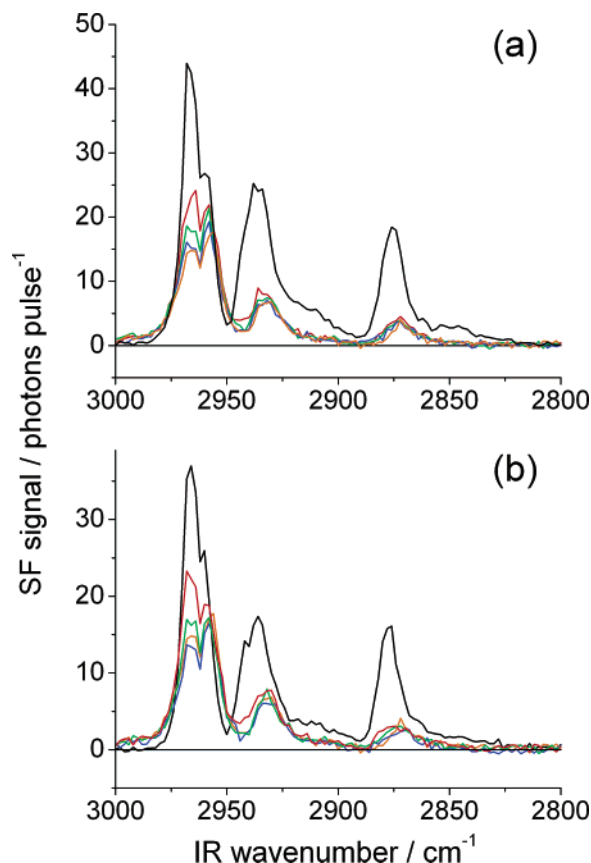


**Figure 11.** (a) ppp sum-frequency spectra of zinc-arachidate at the sapphire–silica interface recorded with increasing pressure: 37 (red), 40 (green), 43.7 (blue), and 46 (orange) MPa. The pre-contact spectrum (divided by 1.5) has been included (black) for comparison. (b) ppp sum-frequency spectra of zinc-arachidate at the sapphire-silica interface recorded with decreasing pressure: 46 (orange), 43 (blue), 40 (green), and 37 (red) MPa. The black line is the post-contact spectrum (divided by 1.5).

constant, but the  $r^-$  mode disappears (as seen in the earlier ssp spectra in Figures 3–5). Overall, the intensity of the ssp spectrum decreased with increasing pressure (Figure 10a) but did not increase again when the pressure was reduced: increasing the applied pressure caused irreversible changes in the monolayer. There is no indication of any increase in the intensity of the  $d^+$  or  $d^-$  modes; increasing pressure does not cause an increase in conformational disorder. The sps spectra (not shown) also show an irreversible decrease in signal strength with increasing pressure.

The spectra for the ppp polarization combination, shown in Figure 11, are more interesting. As in the case of the ssp and sps spectra, there is a red shift in the  $r^+$  and  $r^+_{FR}$  peaks in contact, an irreversible decrease in the intensity of these peaks, and no increase in conformational disorder with increasing pressure. The antisymmetric methyl stretch,  $r^-$ , however, shows nearly reversible changes with pressure. Before contact and at the lowest pressure, the high-frequency  $r^-_{ip}$  mode is more intense than the lower frequency  $r^-_{op}$  component. Since the transition dipole moments of the  $r^-_{ip}$  and  $r^-_{op}$  modes are orthogonal to each other, these changes in the  $r^-$  intensities with pressure accompanied by no change in the  $r^+$  mode suggest a pressure-induced twist of the terminal methyl groups, with no change in tilt.

SF spectra of a Zn arachidate monolayer at the sapphire–silica interface under sliding shear are presented in Figure 12 for the ppp polarization combination. The shear experiments

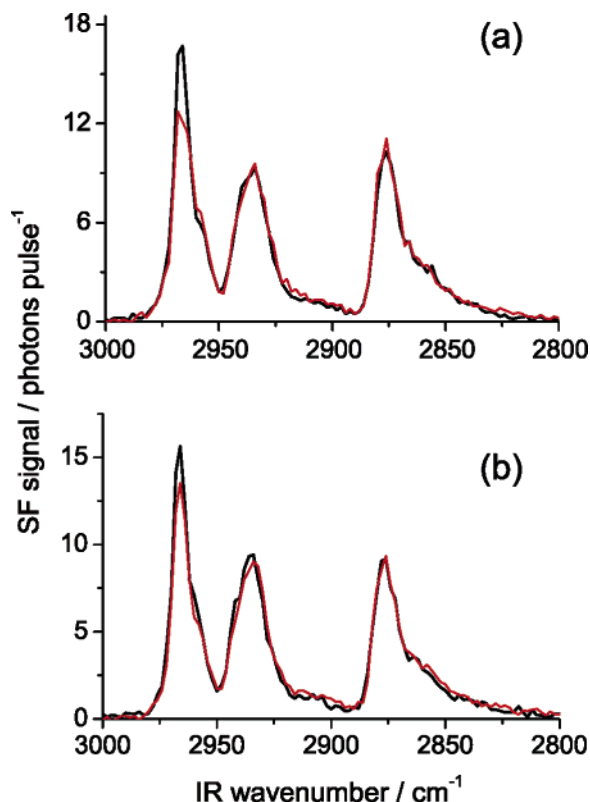


**Figure 12.** ppp sum-frequency spectra of zinc arachidate at the sapphire–silica interface recorded in contact (black) and under shear (red) at (a) shear rate of  $200 \mu\text{m s}^{-1}$  and (b) shear rate of  $1000 \mu\text{m s}^{-1}$ . Normal pressure in contact was 40 MPa.

had to be performed with monolayers on both surfaces; shear experiments with only one monolayer resulted in catastrophic wear of the sample. A deuterated monolayer of Zn arachidate was deposited on the lens surface to ensure that SF signals could be observed and to maintain the integrity of the monolayer on the prism during contact. The SF spectrum in static contact at 40 MPa pressure is shown with a black line and under shear (in the Y-direction) with a red line at a rate of  $200 \mu\text{m s}^{-1}$  (Figure 12a) and  $1 \text{ mm s}^{-1}$  (Figure 12b). The spectra indicate that shear, under these moderate pressures and shear rates, has only a small effect on the structure of the monolayer. Exactly the same spectral change was observed in the spectra, as is seen in the spectra as a function of increasing pressure, namely a drop in the  $r_{\text{ip}}^-$  intensity relative to the rest of the spectral peaks. The intensity drop of the  $r_{\text{ip}}^-$  mode was fully reversible and returned to its pre-shear intensity after shearing was stopped. There was no evidence of wear.

**(vi) Modeling the Effect of Structural Change on SF Spectra.** The standard model for interpreting the SF spectra of organic molecules containing methyl groups<sup>35,57</sup> assumes  $C_{3v}$  symmetry and hence that the normal modes have  $A_1$  ( $r^+$ ) and  $E$  ( $r^-$ ) symmetry. The average local symmetry of a methyl group attached to a hydrocarbon chain is  $C_s$ , with the result that the antisymmetric vibrations have  $A'$  ( $r_{\text{ip}}^-$ ) and  $A''$  ( $r_{\text{op}}^-$ ) symmetry and are not degenerate. Since our observations involve changes in the relative intensities of two resolved antisymmetric modes, they cannot possibly be rationalized under  $C_{3v}$  symmetry. The need to distinguish the two  $r^-$  modes is not unique to the SF spectra of L–B monolayers of fatty acids: high-resolution SF spectra of dodecanol also require nondegenerate antisymmetric stretches for adequate curve fitting.<sup>58</sup> A further simplification that is often invoked in the analysis of SF spectra is free rotation of the methyl group. We note that free rotation does not change

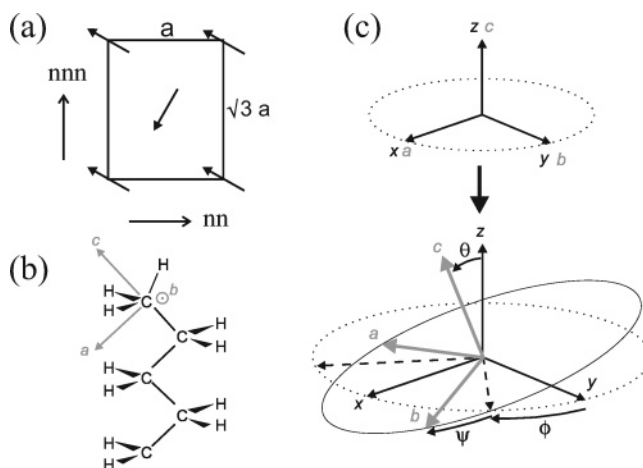


**Figure 13.** (a) Top view of packed upright monolayer, the unit cell is indicated by the dotted line. Arrows show the direction in which the terminal methyl groups are oriented. (b) The end section of an arachidic acid molecule with the molecular axes shown in gray. (c) The transformation between the surface axes and the molecular axes.

the symmetry from  $C_s$  to  $C_{3v}$ , and the antisymmetric modes remain nondegenerate (the methyl group of toluene is a good example). In any event, the barrier to internal rotation is too large ( $4 \text{ kT}$  in ethane at room temperature) to assume free rotation. A better model is a torsional vibration of limited amplitude punctuated by hops over (or tunneling through) the potential barrier on a picosecond time scale. In crystalline alkanes, the degree of torsional motion of the methyl group has been determined from IR spectra:<sup>46</sup> at room temperature the rms torsional angle is only  $10^\circ$ .

A common object of the analysis of SF spectra is to determine the tilt of the methyl group; within the assumption of  $C_{3v}$  symmetry this is all one can do, since the twist of the chain does not affect the normal modes. To relate the angle of the methyl group to that of the chain, one has to assume the direction of tilt; normally this is taken to be in the plane of the hydrocarbon backbone. In monolayer assemblies, however, the local packing is usually a herringbone arrangement with two (or more) molecules per unit cell. In rotator phases (as opposed to crystalline phases) there are no long-range correlations in the twist angle of the chains, but the local packing nevertheless approximates to an orthorhombic perpendicular structure (see Figure 13a).<sup>54</sup> In a rectangular or pseudohexagonal unit cell, the most likely directions of tilt are along one of the unit cell vectors toward either the nearest (crystallographically equivalent) neighbor (nn) or the next nearest neighbor (nnn). For either of these tilts, the direction of tilt is at  $30^\circ$  to the plane of one set of chains and at  $60^\circ$  to the plane of the crystallographically distinct set of chains. Consequently, in determining the effect of a uniform chain tilt on the SF spectra, one has to calculate separately the hyperpolarizability of each inequivalent methyl group in the surface coordinates and then sum the resulting contributions to the susceptibility.

To retain a tractable number of variable parameters, we make a number of simplifying assumptions also: (a) there is no mode mixing, so the normal modes have the same amplitudes as in  $C_{3v}$  symmetry, (b) that the hyperpolarizability elements can be obtained by summing the contributions of individual C–H bonds, (c) that the Raman tensor for the C–H bond is cylindrically symmetric, (d) that the components of the hyperpolarizability that are zero under  $C_{3v}$  symmetry are negligible under  $C_s$  symmetry, (e) the hopping time between minima in the torsional potential is long compared to the transverse

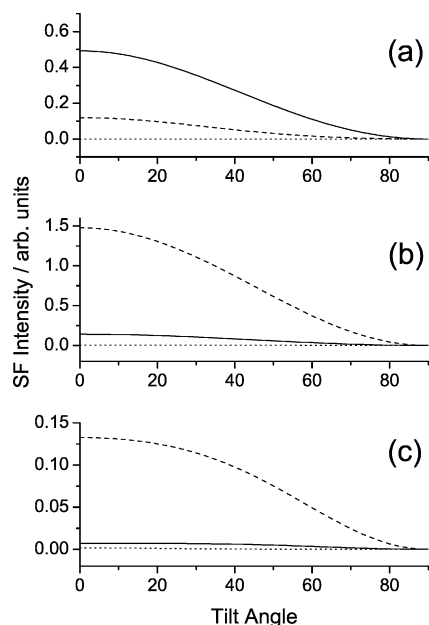


**Figure 14.** Calculated SF intensities for the three observed vibrational modes ( $r^+$ , solid line;  $r_{ip}^-$ , dashed line;  $r_{op}^-$ , dotted line) in the three recorded SF polarization combinations ((a) ssp, (b) ppp, and (c) sps) as a function of tilt angle for molecules in a hexagonal packed monolayer. The calculation was performed for the sapphire/air interface with incident angles of  $55^\circ$  for both lasers.

relaxation time of the vibrational modes. We will assume further that the direction of tilt is random in the laboratory frame, though the restriction of the tilt to a particular direction (e.g., the direction of shear) can be accommodated in the model. The key differences between the model used for this work and the simplified expressions derived by Hirose<sup>35</sup> are (i) nondegenerate antisymmetric modes, (ii) restricted range of torsional angles about the terminal C–C bond, (iii) the use of a lattice with a basis to distinguish between chain tilt and the tilt of the methyl group.

The model is set out in more detail in Appendix B, although a short description of the main points is given here. First, the individual expressions for the molecular hyperpolarizability elements for each vibrational mode are written down.<sup>36</sup> Second, the molecular hyperpolarizability tensor for each mode is averaged over a finite range of torsional angles about the final C–C bond (a nonweighted average over a  $\pm$  twist of moderate magnitude; the average is over all values from 0 to  $\pm\psi$ ). Third, a finite tilt angle is obtained by applying the appropriate rotation matrix for each of the two distinct tilt directions ( $\pm\theta$ ) for each of the two molecules in the unit cell. Averaging these four molecular hyperpolarizabilities for each vibrational mode gives a unit cell hyperpolarizability,  $\beta_{uc}$ , for that mode, for a given tilt angle. The unit cell hyperpolarizability is then averaged in the azimuthal plane to give a lab-frame hyperpolarizability, which is related to  $\chi^{(2)}$  and hence to the SF signal as described earlier. The model has been tested using single molecule tilts in the mirror plane of the molecules, the results of which match those obtained from the tensor transformation elements tabulated by Hirose.<sup>35</sup> Finally, we multiply by the appropriate Fresnel coefficients for the experimental geometry, sum the contributing susceptibility components for each SFG polarization combination (see eqs 3–6), and take the magnitude squared to predict the (relative) SF intensities.

Figure 14 shows calculated intensities for the  $r^+$ ,  $r_{ip}^-$ , and  $r_{op}^-$  vibrational modes in the ssp, ppp, and sps spectra of a Zn arachidate at the sapphire–air interface, as a function of tilt

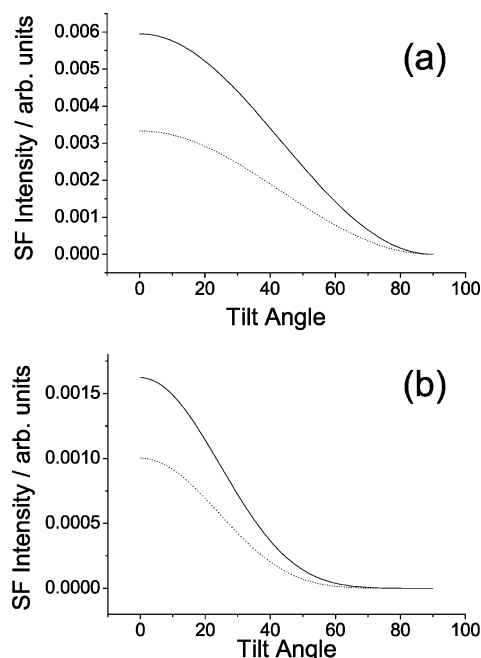


**Figure 15.** Calculated SF intensities for the  $r_{op}^-$  mode in (a) the ppp spectrum and (b) the sps spectrum for two different torsional motions: dotted line for no torsional motion, and solid line for  $\pm 25^\circ$  of torsional motion.

angle. The incident angles of the lasers and the SF emission were set to match those of the experiment. The intensities at zero tilt angle are those expected for the as-deposited monolayer, prior to contact. As can be seen, the model correctly evaluates that the  $r^+$  mode is the most intense peak in the ssp spectrum, followed by the  $r_{ip}^-$  mode. The calculated ppp and sps intensities are also reasonable for the  $r^+$  and  $r_{ip}^-$  modes. However, the calculation does not accurately calculate the intensity of the  $r_{op}^-$  mode in the ppp and sps spectra. The inclusion of twist around the penultimate C–C bond was included in an effort to give more intensity to the  $r_{op}^-$  mode. However, the included  $\pm 25^\circ$  did not have a large impact on the intensity of the mode in the ppp and sps spectra (those for which we see significant intensity in the  $r_{op}^-$  mode; see Figures 3–5). Figure 15 shows the effect of the twist relative to the case where no torsional motion was included in the model for the intensity of the  $r_{op}^-$  mode. As can be seen, the twist does have an effect, almost doubling the calculated intensity. Although this is a significant rise, it is still nowhere near the increase needed to explain the anomalously large  $r_{op}^-$  intensities observed in our SF spectra. It should be noted that the  $r_{op}^-$  mode has intensity with upright chains and no torsional motion, due to the fact that the out-of-plane C–H bonds are not exactly in the plane perpendicular to the chain axis due to the  $\angle CCH$  bond angle chosen for the calculations (see Appendix B).

To obtain a rough estimate of the size of the tilt we could reasonably expect in the system, we can use a simple model for the volume change of the monolayer with pressure.<sup>59</sup>

$$\kappa = -\frac{\delta p}{\delta V/V} \quad (12)$$

where  $\kappa$  is the bulk modulus ( $1/\text{compressibility}$ ),  $\delta p$  is the change in pressure and  $\delta V$  is the change in volume of the material with original volume  $V$ . The ratio  $\delta V/V$  is related to the tilt of the molecules through the following relationship:  $\delta V/V = (1 - \cos \theta)$ , where  $\theta$  is the tilt angle. Using a value for the compressibility of  $9 \times 10^{-10} \text{ Pa}^{-1}$  for  $\kappa$  (the literature value

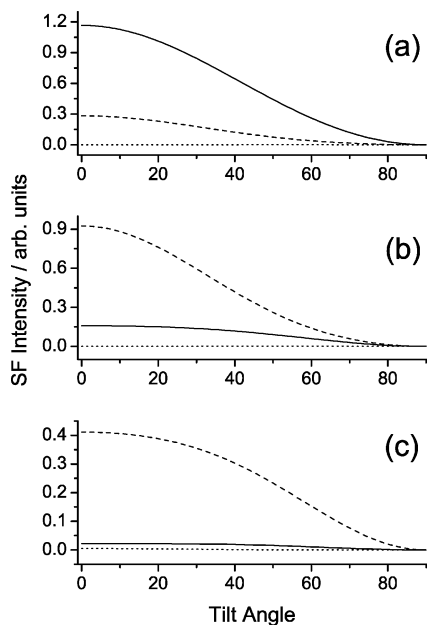


**Figure 16.** Calculated SF intensities for the three observed vibrational modes ( $r^+$ , solid line;  $r_{ip}^-$ , dashed line;  $r_{op}^-$ , dotted line) in the three recorded SF polarization combinations ((a) ssp, (b) ppp, and (c) sps) as a function of tilt angle for molecules in a hexagonal packed monolayer. The calculation was performed for the sapphire–silica interface with incident angles of  $55^\circ$  for both lasers.

for liquid *n*-hexadecane<sup>60</sup> is  $8.67 \times 10^{-10} \text{ Pa}^{-1}$ ) and a pressure of 60 MPa (the pressure achieved by pressing the lens against the prism), we obtain a tilt of  $19^\circ$ . This value is an upper limit, as we expect a solid monolayer to have a smaller compressibility than hexadecane.

Figure 16 shows calculated intensities for the three vibrational modes in the SF spectra for a monolayer at the sapphire–silica interface, as a function of tilt angle, taking into account the different Fresnel coefficients at these two interfaces. The intensities of the theoretical peaks at zero tilt angle for the monolayer at the sapphire–silica interface are, in the main, larger than those determined at the sapphire–air interface, as expected given the Fresnel coefficients for this system (see Table 2). More important than comparing the intensities at zero tilt angle is determining the magnitude of tilt required to produce intensity decreases such as those observed in the spectra of the monolayer upon going from the sapphire–air interface to the sapphire–silica interface. The magnitude of tilt required to produce the observed intensity decreases in-contact can be estimated from a comparison of the model intensities with the actual peak intensities of the  $r^+$  mode in the ssp and ppp spectra at the sapphire–air and sapphire–silica interfaces. In Table 1, the intensity of the  $r^+$  mode in the ppp spectrum at the sapphire–silica interface is approximately 7 times smaller than the  $r^+$  mode intensity at the sapphire–air interface. In the ssp spectra, there is a 9-fold decrease in intensity. To obtain these changes in the model would require a tilt of between  $70^\circ$  and  $80^\circ$ , which is not physically plausible. The theoretical model therefore cannot explain the large in-contact signal drop seen in our spectra and those of other authors.<sup>26,30,31</sup>

Although the model does not explain the absolute strengths of the peaks in the SF spectra, it does provide some insight into how the relative strengths of peaks change under different experimental conditions. Figure 17 plots the intensity of the  $r_{ip}^-$  mode relative to the  $r^+$  mode as a function of tilt for the monolayer at the sapphire–silica interface for the ssp and ppp spectra. In both cases, increasing tilt causes a drop in intensity

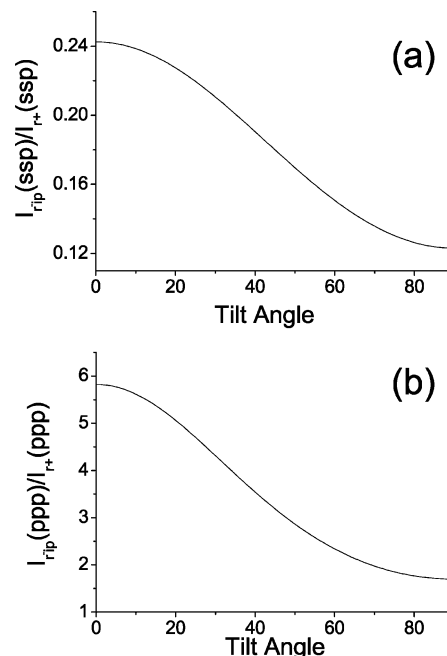


**Figure 17.** (a) The ratio of the  $r_{ip}^-$  mode intensity to the  $r^+$  mode intensity for the ssp spectrum as a function of tilt angle for a monolayer at the sapphire–silica interface, and (b) the ratio of the  $r_{ip}^-$  mode intensity to the  $r^+$  mode intensity for the ppp spectrum as a function of tilt angle for a monolayer at the sapphire–silica interface.

of the  $r_{ip}^-$  mode relative to the  $r^+$  mode. The ssp spectra shown in Figures 3 and 4, along with the fitted peak intensities in Table 1, show that the  $r_{ip}^-$  mode loses intensity relative to the  $r^+$  mode upon contact. This trend is also seen in the ssp spectra as a function of increasing and decreasing pressure shown in Figure 10. The change in  $r_{ip}^-$  peak intensity in the ssp spectra is reversible, as can be seen in Figure 5 and Figure 10b. A small tilt of the chains in the monolayer upon contact (and the application of pressure) yields the appropriate change in the relative intensity of the monolayer based on the model calculation. The model also can explain the reversible drop in intensity of the  $r_{ip}^-$  mode relative to the  $r^+$  mode in the varying pressure ppp spectra shown in Figure 11. The same reasoning can be used to account for the (minor) drop in the intensity  $r_{ip}^-$  mode with shear shown in Figure 12. A small reversible tilt of the hydrocarbon chains under pressure and shear is thus consistent with these spectral changes.

## Conclusions

The spectra we have presented here represent a significant development in our efforts to obtain direct in situ structural information from a monolayer acting as a boundary lubricant. We have demonstrated that SF spectroscopy is a valuable technique for probing monolayers in a tribological contact, but also that serious issues remain in the quantitative interpretation of the spectra. We have observed reversible peak shifts in SF spectra when the monolayer is placed in contact, confirming our assumption, based on the flatness of the surfaces, that the monolayer is in actual mechanical contact with the counterface. We have shown that there is no gross conformational disorder in the monolayer during or after the application of pressure, but that transfer of material between the two surfaces does occur. The reconstruction of the deposited LB film on one face of the sapphire prism has been observed, probably due to the formation of a monolayer in epitaxy with the substrate. The application of pressure drives a phase transformation back to a structure



that resembles the initial upright, hexagonal phase. Small reversible changes observed under shear or loading/unloading of the contact can be rationalized by a small tilt of the hydrocarbon chains.

We have developed a more realistic model for SF spectra of hydrocarbon chain systems that includes the local packing of the chains and the limited torsional motion about the terminal methyl group. Even within this improved model, some aspects of the intensities of the peaks in the SF spectra cannot be predicted, notably the low signal level in contact and the intensity present in the  $r_{\text{op}}^-$  mode. This lack of agreement suggests that there are important features that are still missing from the model.

**Acknowledgment.** The authors wish to thank the EPSRC, the Leverhulme Trust, and the British Ramsay Memorial Fellowship Trust for funding this work.

## Appendix A – Complex Fresnel Coefficients

The Fresnel coefficients ( $K$ ) relate the strength of the incident electric fields to the strength of the field at the interface.<sup>20</sup> They depend on the angles of incidence of the two input wavelengths, on the refractive indices of the two bulk media, and on the dielectric properties of the molecules at the interface.  $L$  is a parameter, similar to  $K$ , that relates the electric field in the emitted SF light to the polarization of the sample at the sum frequency.<sup>21</sup> The equations for the Fresnel coefficients, expressed along the Cartesian axes of the surface and corrected to account for the electric field in the monolayer, are as follows:

$$K_{\text{p},x}^t = \frac{2n_i \cos \theta_i \cos \theta_t}{n_i \cos \theta_i + n_t \cos \theta_t} \quad (\text{A-1})$$

$$K_{\text{s},y}^t = \frac{2n_i \cos \theta_i}{n_i \cos \theta_i + n_t \cos \theta_t} \quad (\text{A-2})$$

$$K_{\text{p},z}^t = \left(\frac{n_t}{n'}\right) \frac{2n_i \cos \theta_i \cos \theta_t}{n_i \cos \theta_i + n_t \cos \theta_t} \quad (\text{A-3})$$

$$L_{\text{p},x}^r = 4\pi i \frac{\omega_{\text{sum}}}{c} \frac{\cos \theta_t}{n_i \cos \theta_r + n_t \cos \theta_t} \quad (\text{A-4})$$

$$L_{\text{s},y}^r = 4\pi i \frac{\omega_{\text{sum}}}{c} \frac{1}{n_i \cos \theta_r + n_t \cos \theta_t} \quad (\text{A-5})$$

$$L_{\text{p},z}^r = 4\pi i \frac{\omega_{\text{sum}}}{c} \left(\frac{n_t}{n'}\right)^2 \frac{\sin \theta_t}{n_i \cos \theta_r + n_t \cos \theta_t} \quad (\text{A-6})$$

The parameters with a subscript  $i$  refer to the incident medium and those with a subscript  $t$  refer to the transmitted medium;  $n'$  is the refractive index of the monolayer. The above equations can be used only when the incident angles are below those of the critical angle for the interface. The sign of the  $K_{\text{p},x}$  and  $K_{\text{p},z}$  terms are different for the visible and infrared wavelengths due to the counter propagating geometry. For the incident infrared light, both  $K_{\text{p},x}$  and  $K_{\text{p},z}$  are negative, and for the incident visible light,  $K_{\text{p},x}$  is negative.

Above the critical angle, the transmitted Fresnel coefficients for the incident beams and the Fresnel coefficient for the SF beam are complex quantities. The equations for the real and imaginary parts of the complex Fresnel coefficients can be obtained from Snell's law and the trigonometric identity  $\cos^2 \theta$

+  $\sin^2 \theta = 1$ . The real and imaginary parts of the Fresnel coefficients are as follows:

$$\text{Re}(K_{\text{p},x}^t) = \frac{2 \cos \theta_i (\sin^2 \theta_i - n_{ii}^2)}{n_{ii}^4 \cos^2 \theta_i + \sin^2 \theta_i - n_{ii}^2} \quad (\text{A-7})$$

$$\text{Im}(K_{\text{p},x}^t) = \frac{2n_{ii}^2 \cos \theta_i (\sin^2 \theta_i - n_{ii}^2)^{1/2}}{n_{ii}^4 \cos^2 \theta_i + \sin^2 \theta_i - n_{ii}^2} \quad (\text{A-8})$$

$$\text{Re}(K_{\text{s},y}^t) = \frac{2 \cos^2 \theta_i}{1 - n_{ii}^2} \quad (\text{A-9})$$

$$\text{Im}(K_{\text{s},y}^t) = \frac{-2 \cos \theta_i (\sin^2 \theta_i - n_{ii}^2)^{1/2}}{1 - n_{ii}^2} \quad (\text{A-10})$$

$$\text{Re}(K_{\text{p},z}^t) = \left(\frac{n_t}{n'}\right)^2 \frac{-2 \cos \theta_i \sin \theta_i (\sin^2 \theta_i - n_{ii}^2)^{1/2}}{n_{ii}^4 \cos^2 \theta_i + \sin^2 \theta_i - n_{ii}^2} \quad (\text{A-12})$$

$$\text{Re}(L_{\text{p},x}^r) = 4\pi \frac{\omega_{\text{sum}}}{c} \frac{-n_{ii}^2 \cos \theta_r (\sin^2 \theta_r - n_{ii}^2)^{1/2}}{n_i (n_{ii}^4 \cos^2 \theta_r + \sin^2 \theta_r - n_{ii}^2)} \quad (\text{A-13})$$

$$\text{Im}(L_{\text{p},x}^r) = 4\pi \frac{\omega_{\text{sum}}}{c} \frac{(\sin^2 \theta_r - n_{ii}^2)}{n_i (n_{ii}^4 \cos^2 \theta_r + \sin^2 \theta_r - n_{ii}^2)} \quad (\text{A-14})$$

$$\text{Re}(L_{\text{s},y}^r) = 4\pi \frac{\omega_{\text{sum}}}{c} \frac{(\sin^2 \theta_r - n_{ii}^2)^{1/2}}{n_i (1 - n_{ii}^2)} \quad (\text{A-15})$$

$$\text{Im}(L_{\text{s},y}^r) = 4\pi \frac{\omega_{\text{sum}}}{c} \frac{\cos \theta_r}{n_i (1 - n_{ii}^2)} \quad (\text{A-16})$$

$$\text{Re}(L_{\text{p},z}^r) = 4\pi \frac{\omega_{\text{sum}}}{c} \left(\frac{n_t}{n'}\right) \frac{\sin \theta_r (\sin^2 \theta_r - n_{ii}^2)^{1/2}}{n_i (n_{ii}^4 \cos^2 \theta_r + \sin^2 \theta_r - n_{ii}^2)} \quad (\text{A-17})$$

$$\text{Im}(L_{\text{p},z}^r) = 4\pi \frac{\omega_{\text{sum}}}{c} \left(\frac{n_t}{n'}\right) \frac{n_{ii}^2 \sin \theta_r \cos \theta_r}{n_i (n_{ii}^4 \cos^2 \theta_r + \sin^2 \theta_r - n_{ii}^2)} \quad (\text{A-18})$$

The subscripts in the above equations have the same meaning as before;  $n_{ii} = n_t/n_i$ . The sign changes mentioned above have to be carried through to the complex Fresnel coefficients. The overall Fresnel factors,  $F_{\text{yyz}}$  etc., at the sapphire–air interface can be calculated using straightforward complex number algebra.

## Appendix B – SF Intensity Modeling

If one assumes that the C–H bonds in the end methyl group of a fatty acid are equivalent and that the modes are not coupled, it is possible to relate the  $\beta_v$  elements for the vibrations of the methyl group to the bond dipole moment derivative ( $\partial\mu/\partial q$ ), the bond polarizability derivative ( $\partial\alpha/\partial q$ ) and the  $\angle\text{CCH}$  bond angle,  $\tau$  ( $= 111^\circ$ ).<sup>36,57,61</sup> By so doing we can obtain expressions for each of the 27 elements of  $\beta_v$  for each mode. In practice there is no need to obtain all 27 expressions, as we can use symmetry to reduce the number of nonzero elements of  $\beta_v$ . With  $C_s$  symmetry, the vibrations of the methyl group are split into

two groups depending upon the irreducible representation to which they belong,  $A'$  or  $A''$ . The  $r^+$  mode and the  $r^-_{ip}$  mode are both  $A'$  vibrations, and the  $r^-_{op}$  mode is an  $A''$  vibration. The nonzero  $\beta_v$  tensor elements for  $A'$  are  $\beta_{aaa}$ , ( $=\beta_{bba}$ ),  $\beta_{aca}$  ( $=\beta_{caa}$ ),  $\beta_{acc}$  ( $=\beta_{cac}$ ),  $\beta_{aac}$  ( $=\beta_{bbc}$ ),  $\beta_{ccc}$ , and  $\beta_{cca}$ . For  $A''$ , the nonzero tensor elements are  $\beta_{bcb}$  ( $=\beta_{cbb}$ ) and  $\beta_{bab}$  ( $=\beta_{abb}$ ). To reduce the level of complexity and to separate the two  $A'$  vibrations, we assume that the elements that are zero for the  $A_1$  irreducible representation in  $C_{3v}$  symmetry will be negligible for the  $r^+$  mode in  $C_s$  symmetry and that the elements that are zero for the E representation in  $C_{3v}$  symmetry will be negligible for the  $r^-_{ip}$  mode in  $C_s$  symmetry. This leaves  $\beta_{ccc}$  and  $\beta_{aac}$  ( $=\beta_{bbc}$ ) for the  $r^+$  mode,  $\beta_{aaa}$  and  $\beta_{aca}$  ( $=\beta_{caa}$ ) for the  $r^-_{ip}$  mode, and  $\beta_{bcb}$  ( $=\beta_{cbb}$ ) and  $\beta_{bab}$  ( $=\beta_{abb}$ ) for the  $r^-_{op}$  mode.

Only relative intensities of the vibrational modes are required from the model, therefore we do not need to have values for the bond dipole moment derivative ( $\partial\mu/\partial q$ ) and the bond polarizability derivative ( $\partial\alpha/\partial q$ ). The relative intensities of the relevant  $\beta_v$  elements are as follows.<sup>36</sup>  $r^+$  mode:

$$\beta_{aac} \propto -\frac{\sqrt{3}}{2} \cos \tau ((1+t) + \cos^2 \tau (t-1)) \quad (B-1)$$

$$\beta_{ccc} \propto -\sqrt{3} \cos \tau (\cos^2 \tau (1+t) + t) \quad (B-2)$$

$r^-_{ip}$  mode:

$$\beta_{aaa} \propto -\frac{3}{4} (1+t) \sin^3 \tau \quad (B-3)$$

$$\beta_{caa} \propto -\frac{3}{2} (1+t) \sin^2 \tau \cos \tau \quad (B-4)$$

$r^-_{op}$  mode:

$$\beta_{bab} \propto -\frac{3}{4} (1-t) \sin^3 \tau \quad (B-5)$$

$$\beta_{bcb} \propto -\frac{3}{2} (1-t) \sin^2 \tau \cos \tau \quad (B-6)$$

where  $t$  is a ratio of elements from the polarizability derivative tensor,  $\alpha'_{aa}/\alpha'_{cc}$ , which can be related to the hyperpolarizability ratio,  $r$  ( $=\beta_{aa}/\beta_{cc}$ ). The value of  $t$  in the calculations in this work is chosen to be zero, i.e., the bonds have zero polarizability perpendicular to the bond axis. This is one extreme in the range of possible  $t$  values, giving a value of 3.4 for the hyperpolarizability ratio,  $r$ . This value of  $r$  has been used by other authors in calculations of SF intensities.<sup>30,47</sup>

The molecular hyperpolarizability tensor needs to undergo a transformation to obtain a lab-frame hyperpolarizability tensor. The transformation can be viewed as follows. If we denote the lab-frame axes as  $x$ ,  $y$ , and  $z$  and the molecular axes as  $a$ ,  $b$ , and  $c$ , then the molecular axes can be obtained by rotating the  $abc$  axes around  $z$  by an angle  $\phi$ , tilting the  $abc$  axes an angle  $\theta$  away from the  $z$  axes toward the  $a$  axis, and rotating the  $abc$  axes by and angle  $\psi$  around the  $c$  axis (see Figure 13c). The calculation of tensor elements in the new reference frame involves the following expression:

$$\beta_{(ijk)} = \sum_{lmn} U_{ijk:lmn} \beta_{(lmn)} \quad (B-7)$$

where  $\beta_{(ijk)}$  is the new tensor element and  $U_{ijk:lmn}$  is a combination of rotation matrix terms taken from the following rotation matrix:<sup>61</sup>

$$\begin{pmatrix} \cos(\psi)\cos(\theta)\cos(\phi) - \sin(\psi)\sin(\phi) & \sin(\psi)\cos(\theta)\cos(\phi) + \sin(\phi)\cos(\psi) & -\cos(\phi)\sin(\theta) \\ -\sin(\phi)\cos(\theta)\cos(\psi) - \cos(\phi)\sin(\psi) & -\sin(\phi)\cos(\theta)\cos(\psi) + \cos(\psi)\sin(\phi) & \sin(\phi)\sin(\theta) \\ \sin(\theta)\cos(\psi) & \sin(\theta)\sin(\psi) & \cos(\theta) \end{pmatrix} \quad (B-8)$$

The term  $U_{ijk:lmn}$  is a product of three terms from the matrix linking each tensor element in the old reference frame with a single element in the new reference frame.

The exact calculation in this model is slightly more complicated as there is a transformation of the molecular hyperpolarizability prior to the lab-frame transformation to take into account some degree of frustrated rotation of the end methyl group around the terminal C–C bond of the hydrocarbon chains. Many authors assume free rotation of the end methyl group, which itself assumes that the barrier to rotation is lower than  $kT$ . This assumption is used to simplify the symmetry of the end methyl group to  $C_{3v}$ . The torsional potential of the end methyl group is likely to be of similar magnitude to that of ethane, meaning that  $kT$  is around 4 times too small to allow free rotation. We assume that the torsional potential of the end methyl group gives rise to a tilt of approximately  $\pm 25^\circ$  (this is larger than the value of  $\pm 10^\circ$  determined by MacPhail et al.; however, a larger value was chosen to magnify any effects of torsion on the SF intensities. This rotation is applied to  $\beta_v$  using eq B-7 and a  $c$ -axis rotation matrix for rotation around the last C–C bond (see Figure 13b):

$$\begin{pmatrix} \cos\gamma & \sin\gamma & 0 \\ -\sin\gamma & \cos\gamma & 0 \\ 0 & 0 & 1 \end{pmatrix} \quad (B-9)$$

The new  $\beta_v$  tensor for each mode is taken as an unweighted average of the  $\beta_v$  tensors calculated at each angle of rotation.

Another complication in this model is that there are two separate contributions to the unit cell hyperpolarizability, one from each of the half-molecules in the hexagonally packed unit cell (see Figure 13a). Each of the molecules has a different value for  $\phi$  and therefore each molecule will give a slightly different contribution to the unit cell hyperpolarizability. The following equation is used for the transformation to take both molecules into account:

$$\beta_{uc,v(ijk)} = \left( \sum_{lmn} U_{ijk:lmn} \beta_{v(lmn)} (1) + \sum_{lmn} U_{ijk:lmn} \beta_{v(lmn)} (2) \right) \quad (B-10)$$

In terms of the unit cell, the tilt angle,  $\theta$ , is initially set at  $35^\circ$ , the angle of tilt for a terminal methyl group on an upright hydrocarbon chain. The azimuthal angle,  $\phi$ , is set differently for the two molecules in the unit cell, aligning the molecules to be at  $30^\circ$  and  $-60^\circ$  relative to one of the two possible directions of tilt (based on space filling considerations the tilt direction will be toward the nearest neighbor (tilt direction nn) or toward the next-nearest neighbor (tilt direction nnn), see Figure 13a). The final angle,  $\psi$ , is initially set to zero with the methyl group in the minimum energy conformation (staggered) with respect to the first methylene group on the hydrocarbon chain.  $\beta_{uc}$  can be obtained for any initial configuration of the molecule in the unit cell. The final step in calculating a lab frame hyperpolarizability is to average over all azimuthal angles for the unit cell hyperpolarizability. This is a simple nonweighted average over  $360^\circ$ , using a  $z$ -axis rotation matrix (such as eq B-9). The model uses these lab-frame hyperpolarizabilities as proportional to the lab-frame susceptibility tensor, enabling one to calculate the relative intensities of vibrational modes using eqs 3–6 in the main body of the paper and the Fresnel

coefficients given in Appendix A. Tilting of the molecules is directly included as a variable in the calculation of the unit cell hyperpolarizability. The average of the tilts in the positive and negative directions is used in the calculation as there is no imperative to choose one sign of tilt over another. In addition, an average is taken of molecules tilting in either the nn or nnn direction, as there is no imperative to choose one direction of tilt over another.

## References and Notes

- (1) Bowden, F. P.; Tabor, D. *The friction and lubrication of solids*; Clarendon Press: Oxford, 1950.
- (2) Maboudian, R. *Surf. Sci. Rep.* **1998**, *30*, 207.
- (3) Bhushan, B.; Israelachvili, J. B.; Landman, U. *Nature (London)* **1995**, *374*, 607.
- (4) Bain, C. D.; Whitesides, G. M. *Angew. Chem.* **1989**, *101*, 522.
- (5) Ulman, A. *An introduction to ultrathin organic films: from Langmuir-Blodgett to self-assembly*; Academic Press: Boston, 1991.
- (6) Petty, M. C. *Langmuir Blodgett Films*; Cambridge University Press: Cambridge, 1997.
- (7) Yamada, S.; Israelachvili, J. J. *J. Phys. Chem. B* **1998**, *102*, 234.
- (8) Yoshizawa, H.; Israelachvili, J. J. *J. Phys. Chem.* **1993**, *97*, 11300.
- (9) Kim, H. I.; Koini, T.; Lee, T. R.; Perry, S. S. *Langmuir* **1997**, *13*, 7192.
- (10) Xiao, X.; Hu, J.; Charych, D. H.; Salmeron, M. *Langmuir* **1996**, *12*, 235.
- (11) Khatri, O. P.; Bain, C. D.; Biswas, S. K. *J. Phys. Chem. B* **2005**, *109*, 23405.
- (12) Glosli, J. N.; McClelland, G. M. *Phys. Rev. Lett.* **1993**, *70*, 1960.
- (13) Koike, A.; Yoneya, M. *J. Phys. Chem. B* **1998**, *102*, 3669.
- (14) Koike, A.; Yoneya, M. *Langmuir* **1997**, *13*, 1718.
- (15) Koike, A.; Yoneya, M. *J. Chem. Phys.* **1996**, *105*, 6060.
- (16) Tupper, K. J.; Brenner, D. W. *Thin Solid Films* **1994**, *253*, 185.
- (17) Tupper, K. J.; Colton, R. J.; Brenner, D. W. *Langmuir* **1994**, *10*, 2041.
- (18) Mikulski, P. T.; Gao, G.; Chateaufneuf, G. M.; Harrison, J. A. *J. Chem. Phys.* **2005**, *122*, 024701/1.
- (19) Mikulski, P. T.; Harrison, J. A. *J. Am. Chem. Soc.* **2001**, *123*, 6873.
- (20) Mikulski, P. T.; Harrison, J. A. *Tribol. Lett.* **2001**, *10*, 29.
- (21) Bain, C. D. Sum-frequency vibrational spectroscopy of the solid/liquid interface. In *J. Chem. Soc., Faraday Trans.*, 1995; Vol. 91; p 1281.
- (22) Beattie, D. A.; Bain, C. D. Sum-Frequency Spectroscopy. In *Handbook of Vibrational Spectroscopy*; Chalmers, J. M., Griffiths, P. R., Eds.; Wiley: Chichester, 2002; Vol. 1; p 801.
- (23) Williams, C. T.; Beattie, D. A. *Surf. Sci.* **2002**, *500*, 545.
- (24) Duffy, D. C.; Friedmann, A.; Boggis, S. A.; Klenerman, D. *Langmuir* **1998**, *14*, 6518.
- (25) Huang, J. Y.; Song, K. J.; Lagoutchev, A.; Yang, P. K.; Chuang, T. J. *Langmuir* **1997**, *13*, 58.
- (26) Du, Q.; Xiao, X. D.; Charych, D.; Wolf, F.; Frantz, P.; Shen, Y. R.; Salmeron, M. *Phys. Rev. B, Condens. Matter* **1995**, *51*, 7456.
- (27) Fraenkel, R.; Butterworth, G. E.; Bain, C. D. *J. Am. Chem. Soc.* **1998**, *120*, 203.
- (28) Beattie, D. A.; Haydock, S.; Bain, C. D. *Vibr. Spectrosc.* **2000**, *24*, 109.
- (29) Haydock, S. A.; Bain, C. D. *Abstracts of Papers*, 225th ACS National Meeting, New Orleans, LA, United States, March 23–27, 2003 **2003**, COLL.
- (30) Berg, O.; Klenerman, D. *J. Am. Chem. Soc.* **2003**, *125*, 5493.
- (31) Berg, O.; Klenerman, D. *J. Appl. Phys.* **2001**, *90*, 5070.
- (32) Eisert, F.; Gurka, M.; Legant, A.; Buck, M.; Grunze, M. *Science* **2000**, *287*, 468.
- (33) Shen, Y. R. *The Principles of Nonlinear Optics*; John Wiley & Sons: New York, 1984.
- (34) Born, M.; Wolf, E. *Principles of optics: electromagnetic theory of propagation, interference and diffraction of light*, 7th (expanded) ed.; Cambridge University Press: Cambridge, 1999.
- (35) Hirose, C.; Akamatsu, N.; Domen, K. *Appl. Spectrosc.* **1992**, *46*, 1051.
- (36) Potterton, E. Sum-frequency spectroscopy of adsorbates on crystal surfaces. Ph.D. Thesis, University of Oxford, 1997.
- (37) Blodgett, K. B. *J. Am. Chem. Soc.* **1935**, *57*, 1007.
- (38) Blodgett, K. B.; Langmuir, I. *Phys. Rev.* **1937**, *51*, 964.
- (39) Heavens, O.; Ditchburn, R. *Insight into Optics*; Wiley: Chichester, 1991.
- (40) Johnson, K. L. *Contact mechanics*, 1st paperback ed.; Cambridge University Press: Cambridge, 1987.
- (41) Rabinowitz, P.; Perry, B. N.; Levinos, N. *IEEE J. Quantum Electron.* **1986**, *QE-22*, 797.
- (42) Bain, C. D.; Davies, P. B.; Ong, T. H.; Ward, R. N.; Brown, M. A. *Langmuir* **1991**, *7*, 1563.
- (43) Armstrong, B. H. *J. Quantitative Spectrosc. Radiat. Transfer* **1967**, *7*, 61.
- (44) Drayson, S. R. *J. Quantitative Spectrosc. Radiat. Transfer* **1976**, *16*, 611.
- (45) Parratt, L. G. *Phys. Rev.* **1954**, *95*, 359.
- (46) MacPhail, R. A.; Strauss, H. L.; Snyder, R. G.; Elliger, C. A. *J. Phys. Chem.* **1984**, *88*, 334.
- (47) Bell, G. R.; Bain, C. D.; Ward, R. N. *J. Chem. Soc., Faraday Trans.* **1996**, *92*, 515.
- (48) Hirose, C.; Yamamoto, H.; Akamatsu, N.; Domen, K. *J. Phys. Chem.* **1993**, *97*, 10064.
- (49) Ong, T. H.; Davies, P. B.; Bain, C. D. *Langmuir* **1993**, *9*, 1836.
- (50) Stole, S. M.; Porter, M. D. *Langmuir* **1990**, *6*, 1199.
- (51) Rideal, E. K.; Tadayon, J. *Proc. R. Soc. (London)* **1954**, *A225*, 346.
- (52) Meyer, E.; Overney, R.; Brodbeck, D.; Howald, L.; Luethi, R.; Frommer, J.; Guentherodt, H. *J. Phys. Rev. Lett.* **1992**, *69*, 1777.
- (53) Riviere, S.; Henon, S.; Meunier, J.; Schwartz, D. K.; Tsao, M. W.; Knobler, C. M. *J. Chem. Phys.* **1994**, *101*, 10045.
- (54) Small, D. *The Physical Chemistry of Lipids*; Plenum Press: New York, 1986.
- (55) Berman, A. D.; Ducker, W. A.; Israelachvili, J. N. *Langmuir* **1996**, *12*, 4559.
- (56) Bordarier, P.; Schoen, M.; Fuchs, A. H. *Phys. Rev. E* **1998**, *57*, 1621.
- (57) Hirose, C.; Akamatsu, N.; Domen, K. *J. Chem. Phys.* **1992**, *96*, 997.
- (58) Casson, B. D.; Braun, R.; Bain, C. D. *Faraday Discuss.* **1997**, *104*, 209.
- (59) Massey, B. S. *Mechanics of fluids*, 6th ed.; Chapman & Hall: London, 1989.
- (60) Weast, R. C. *CRC handbook of chemistry and physics*, 1st Student ed.; CRC Press: Boca Raton, FL, 1988.
- (61) Wilson, E. B.; Decius, J. C.; Cross, P. C. *Molecular vibrations: the theory of infrared and Raman vibrational spectra*; Dover Publications: New York, 1980.